JWST Observations of SN 2023ixf II: The Panchromatic Evolution Between 250 and 720 Days After the Explosion

K. Medler,[1] C. Ashall,[1] P. Hoeflich,[2] E. Baron,[3,4] J. M. DerKacy,[5] M. Shahbandeh,[5] T. Mera,[2]

C. M. Pfeffer,[1,*] W. B. Hoogendam,[1,*] D. O. Jones,[6] S. Shiber,[2] E. Fereidouni,[2] O. D. Fox,[5] J. Jencson,[7] L. Galbany,[8,9] J. T. Hinkle,[1,†] M. A. Tucker,[10,11] B. J. Shappee,[1] M. E. Huber,[1] K. Auchettl,[12,13] C. R. Angus,[14,15] D. D. Desai,[1] A. Do,[16] A. V. Payne,[5] J. Shi,[12] M. Y. Kong,[1] S. Romagnoli,[12] A. Syncatto,[17] G. Clayton,[18,19] M. Dulude,[5] M. Engesser,[5] A. V. Filippenko,[20] S. Gomez,[21] E. Y. Hsiao,[2] T. de Jaeger,[22] J. Johansson,[23] K. Krisciunas,[24] S. Kumar,[25] J. Lu,[26] M. Matsuura,[27] P. A. Mazzali,[28,29] D. Milisavljevic,[30] N. Morrell,[31] R. O'Steen,[5] S. Park,[32] M. M. Phillips,[31] A. P. Ravi,[33] A. Rest,[5,34] J. Rho,[35] N. B. Suntzeff,[24] A. Sarangi,[35] N. Smith,[36] M. D. Stritzinger,[37] L. Strolger,[5] T. Szalai,[38,39] T. Temim,[40] S. Tinyanont,[41] S. D. Van Dyk,[7] L. Wang,[24] Q. Wang,[42] R. Wesson,[27] Y. Yang,[43,20] and S. Zsíros[44,45]

[1] *Institute for Astronomy, University of Hawai'i at Manoa, 2680 Woodlawn Dr., Hawai'i, HI 96822, USA*

[2] *Department of Physics, Florida State University, Tallahassee, FL 32306, USA*

[3] *Planetary Science Institute, 1700 East Fort Lowell Road, Suite 106, Tucson, AZ 85719-2395, USA*

[4] *Hamburger Sternwarte, Gojenbergsweg 112, D-21029 Hamburg, Germany*

[5] *Space Telescope Science Institute, 3700 San Martin Drive, Baltimore, MD 21218-2410, USA*

[6] *Institute for Astronomy, University of Hawai'i, 640 N. A'ohoku Pl., Hilo, HI 96720, USA*

[7] *Caltech/IPAC, Mailcode 100-22, Pasadena, CA 91125, USA*

[8] *Institute of Space Sciences (ICE, CSIC), Campus UAB, Carrer de Can Magrans, s/n, E-08193 Barcelona, Spain*

[9] *Institut d'Estudis Espacials de Catalunya (IEEC), E-08034 Barcelona, Spain*

[10] *Center for Cosmology and Astroparticle Physics, The Ohio State University, Columbus, OH, USA*

[11] *Department of Astronomy, The Ohio State University, Columbus, OH, USA*

[12] *Ozgrav, School of Physics, The University of Melbourne, Parkville, VIC 3010, Australia*

[13] *Department of Astronomy and Astrophysics, University of California, Santa Cruz, CA 95064, USA*

[14] *Astrophysics Research Centre, School of Mathematics and Physics, Queen's University Belfast, Belfast BT7 1NN, UK*

[15] *DARK, Niels Bohr Institute, University of Copenhagen, Jagtvej 128, DK-2200 Copenhagen Ø Denmark*

[16] *Institute of Astronomy and Kavli Institute for Cosmology, Madingley Road, Cambridge CB3 0HA, UK*

[17] *Department of Physics and Astronomy, University of Hawai'i at Hilo, Hilo, HI, USA*

[18] *Department of Physics & Astronomy, Louisiana State University, Baton Rouge, LA 70803, USA*

[19] *Space Science Institute, 4765 Walnut St, Suite B Boulder, CO 80301, USA*

[20] *Department of Astronomy, University of California, Berkeley, CA 94720-3411, USA*

[21] *Department of Astronomy, The University of Texas at Austin, 2515 Speedway, Stop C1400, Austin, TX 78712, USA*

[22] *LPNHE, (CNRS/IN2P3, Sorbonne Université, Université Paris Cité), Laboratoire de Physique Nucléaire et de Hautes Énergies, 75005, Paris, France*

[23] *Department of Physics, The Oskar Klein Center, Stockholm University, AlbaNova, 10691 Stockholm, Sweden*

[24] *George P. and Cynthia Woods Mitchell Institute for Fundamental Physics and Astronomy, Department of Physics and Astronomy, Texas A&M University, College Station, TX 77843, USA*

[25] *Department of Astronomy, University of Virginia, 530 McCormick Rd, Charlottesville, VA 22904, USA*

[26] *Department of Physics & Astronomy, Michigan State University, East Lansing, MI, USA*

[27] *Cardiff Hub for Astrophysical Research and Technology (CHART), School of Physics and Astronomy, Cardiff University, The Parade, Cardiff CF24 3AA, UK*

[28] *Astrophysics Research Institute, Liverpool John Moores University, 146 Brownlow Hill, Liverpool L3 5RF, UK*

[29] *Max-Planck-Institut für Astrophysik, Karl-Schwarzschild Straße 1, 85748 Garching, Germany*

[30] *Purdue University, Department of Physics and Astronomy, 525 Northwestern Ave, West Lafayette, IN 4790720, USA*

[31] *Las Campanas Observatory, Carnegie Observatories, Casilla 601, La Serena, Chile*

[32] *Department of Physics and Astronomy, Seoul National University, Gwanak-ro 1, Gwanak-gu, Seoul, 08826, South Korea*

[33] *Department of Physics and Astronomy, University of California, 1 Shields Avenue, Davis, CA 95616-5270, USA*

[34] *Physics and Astronomy Department, Johns Hopkins University, Baltimore, MD 21218, USA*

[35] *SETI Institute, 339 Bernardo Ave., Ste. 200, Mountain View, CA 94043, USA*

[36] *Steward Observatory, University of Arizona, 933 N. Cherry St, Tucson, AZ 85721, USA*

[37] *Department of Physics and Astronomy, Aarhus University, Ny Munkegade 120, DK-8000 Aarhus C, Denmark.*

[38] *Department of Experimental Physics, Institute of Physics, University of Szeged, H-6720 Szeged, Dóm tér 9, Hungary*

[39] *MTA-ELTE Lendület "Momentum" Milky Way Research Group, Szent Imre H. st. 112, 9700 Szombathely, Hungary*

[40] Princeton University, 4 Ivy Lane, Princeton, NJ 08544, USA
[41] National Astronomical Research Institute of Thailand, 260 Moo 4, Donkaew, Maerim, Chiang Mai, 50180, Thailand
[42] Department of Physics and Kavli Institute for Astrophysics and Space Research, Massachusetts Institute of Technology, 77 Massachusetts Avenue, Cambridge, MA 02139, USA
[43] Physics Department, Tsinghua University, Beijing, 100084, China
[44] Department of Experimental Physics, Institute of Physics, University of Szeged, Dóm tér 9, 6720 Szeged, Hungary
[45] HUN-REN CSFK Konkoly Observatory, Konkoly Thege M. ut 15-17, Budapest, 1121, Hungary

(Received July 29, 2025; Revised; Accepted)

Submitted to ApJ

ABSTRACT

We present the nebular phase spectroscopic and photometric observations of the nearby hydrogen-rich core-collapse supernova (CC-SN) 2023ixf, obtained through our *JWST* programs. These observations, combined with ground-based optical and near-infrared spectra, cover $+252.67 - 719.96$ d, creating a comprehensive, panchromatic time-series dataset spanning $0.32 - 30$ μm. In this second paper of the series, we focus on identifying key spectral emission features and tracking their evolution through the nebular phase. The *JWST* data reveal hydrogen emission from the Balmer to Humphreys series, as well as prominent forbidden lines from Ne, Ar, Fe, Co, and Ni. NIRSpec observations display strong emission from the first overtone and fundamental bands of carbon monoxide, which weaken with time as the ejecta cools and dust emission dominates. The spectral energy distribution shows a clear infrared excess emerging by $+252.67$ d peaking around 10.0 μm, with a secondary bump at 18.0 μm developing by $+719.96$ d. We suggest that this evolution could arises from multiple warm dust components. In upcoming papers in this series, we will present detailed modeling of the molecular and dust properties. Overall, this dataset significantly advances our understanding of the mid-infrared properties of CC-SNe, providing an unprecedented view of their late-time line, molecule, and dust emission.

1. INTRODUCTION

Core-collapse supernovae (CC-SNe), which arise from the collapse of massive stars with zero-age main sequence mass $M_{ZAMS} \gtrsim 8$ $M_\odot$, provide crucial insights into the final stages of stellar evolution (Smartt et al. 2009). These explosions enrich galaxies with iron-group and α elements (Woosley & Weaver 1995; Janka 2012; Wang & Burrows 2024), and contribute to the formation of galactic dust (Dwek et al. 2007; Gall et al. 2011). While public, optical, all-sky (e.g., Shappee et al. 2014; Tonry et al. 2018) and targeted (e.g., Huber et al. 2015; Groot et al. 2022; Dyer et al. 2024) surveys now discover thousands of CC-SNe annually, the majority of these events are primarily studied in the optical or near-infrared (NIR), with far fewer observations at the ultraviolet (UV) or mid-infrared (MIR) wavelengths. This observational bias, confined typically to $\sim 0.3 - 2.5$ μm, limits our ability to comprehensively explore the parameter space of the physical conditions, and explosion physics of these objects, as well as their role in galactic chemical and dust enrichment.

The MIR regime, spanning $5 - 30$ μm, remains relatively under-explored in the study of CC-SNe, yet it contains crucial features that are otherwise inaccessible. While strong emission lines are prevalent at all wavelengths, the emission lines located within the optical and NIR can be heavily blended making species identification and modeling more difficult. In contrast, lines at longer wavelengths (≥ 3 μm) tend to be significantly less blended, due to reduced overlap of the Doppler broadened lines, allowing for clearer identification and modeling (e.g., Jerkstrand et al. 2012; Ashall et al. 2024a). Additionally, the IR flux is significantly less affected by extinction from dust along the line of sight, allowing for more accurate spectroscopic modeling. Several strong C, O, Ne, and Na lines are located in the IR along with many Fe, Ni, and Co lines, which dominate at late times (e.g., Kotak et al. 2005, 2006; Jerkstrand et al. 2012). Modeling these IR emission lines provides deeper insight into the progenitor properties than optical modeling alone (e.g., Woosley & Weaver 1995; Jerkstrand et al. 2012).

* National Science Foundation Graduate Research Fellow
† NASA FINESST Future Investigator

MIR observations of SNe offer more than access to unique emission lines; they are essential for tracing dust formation. CC-SNe are predicted to contribute significantly to the large dust masses observed in early universe galaxies (Dwek & Scalo 1980; Wooden et al. 1993; Hughes et al. 1997; Fan et al. 2003; Maiolino et al. 2004; Schneider et al. 2004; Dwek 2006; Gall et al. 2011; Watson et al. 2015), as they form dust considerably faster than Asymptotic Giant Branch Stars, which dominate dust production in the local universe (Ferrarotti & Gail 2006; Valiante et al. 2009; Williams et al. 2014; Maund 2017). Both pre-existing circumstellar dust heated by the explosion and newly formed dust within the SN ejecta emit strongly at NIR and MIR wavelengths, making these regimes crucial for identifying and characterizing dust production in SNe (Ercolano et al. 2007; Kotak et al. 2009; Wesson et al. 2015; Szalai et al. 2019; Sarangi 2022; Shahbandeh et al. 2023).

Before the onset of dust formation, CC-SNe are expected to synthesize molecules of Carbon Monoxide (CO) and Silicon Monoxide (SiO) (Liu et al. 1992; Liu & Dalgarno 1994; Clayton et al. 2001; Biscaro & Cherchneff 2014; Liljegren et al. 2020). Molecules enhance dust formation by acting as nucleation points onto which dust grains can condense (Sluder et al. 2018). Additionally, molecules rapidly cool the ejecta to below the dust condensation point, enabling dust formation (Liu & Dalgarno 1995; Liljegren et al. 2020). This cooling happens through re-emission via the molecular rovibrational bands whose spectral signatures are only located at IR wavelengths, with the first overtone of CO ($\Delta v = 2$) located at $\sim 2.3-2.5$ μm, and the CO and SiO fundamentals ($\Delta v = 1$) located at $\sim 4.3 - 5.2$ μm and $\sim 7.5-9.3$ μm, respectively (Snow & Rideal 1929; Singh 1975). The location, formation rate, and total mass of these molecules are highly dependent on the initial mass of the progenitor and offer a unique probe to constrain the progenitor properties and explosion physics (Woosley et al. 2002; Müller et al. 2016).

Several hydrogen-rich Type-II CC-SNe (SNe II) have displayed molecular features. The CO first overtone was first detected in SN 1987A (Catchpole et al. 1987; Spyromilio et al. 1988; Liu et al. 1992; Wooden et al. 1993) and later in other events via ground-based (GB) NIR spectroscopy (e.g., Spyromilio & Leibundgut 1996; Gerardy et al. 2000; Pozzo et al. 2007; Kotak et al. 2005; Meikle et al. 2011). Limited MIR coverage has resulted in, with the exception of SN 1987A (Wooden et al. 1993), only partial observations of the CO fundamental band (Wooden et al. 1993; Kotak et al. 2005; Szalai et al. 2011). Finally, the SiO fundamental band, typically emerging several months after the CO (Roche et al. 1991), has been identified in several late-time MIR spectra (Wooden et al. 1993; Kotak et al. 2006, 2009; Szalai et al. 2011; Szalai & Vinkó 2013).

Once the ejecta is sufficiently cool, $T \leq 2000$ K, the formation of fresh dust begins (Clayton et al. 2001; Sarangi & Cherchneff 2015; Sluder et al. 2018). Signatures of dust typically emerge as an IR excess observed one hundred days to a few years after the explosion (Roche et al. 1989). A time series of NIR and MIR spectroscopy enables detailed tracking of the evolving IR excess and places constraints on key dust properties (e.g., location, composition, and quantity; Meikle et al. 2007; Kotak et al. 2009; Szalai & Vinkó 2013; Shahbandeh et al. 2023). While hot dust ($T_{\rm dust} \geq 800$ K) can be observed with ground based NIR (GB-NIR) instruments (Pozzo et al. 2004; Tinyanont et al. 2019; Rho et al. 2021; Ravi et al. 2023), cooler dust requires MIR observations (Rho et al. 2021; Shahbandeh et al. 2023; Ravi et al. 2023).

The extraordinary capabilities of *JWST* have dramatically improved our ability to study molecule and dust formation in CC-SNe. *JWST* can simultaneously cover the NIR and MIR regions with the Near-Infrared Spectrograph (NIRSpec, $1.6 - 5.2$ μm) and Mid-Infrared Instrument (MIRI, $4.9 - 30.0$ μm), allowing for comprehensive, simultaneous observations of the CO and SiO emission features, as well as detection of both hot and cool dust in nearby CC-SNe (e.g., Shahbandeh et al. 2023, 2024; Zsíros et al. 2024; Clayton et al. 2025; Shahbandeh et al. 2025).

In this paper, we present *JWST* spectroscopic and photometric observations of SN 2023ixf spanning approximately +250 to +720 d past explosion. The four epochs of spectroscopic data were obtained as part of our programs JWST-DD-4575 and JWST-GO-5290 (Ashall et al. 2023a, 2024b), while the photometric data was acquired through our programs JWST-GO-3921 and JWST-GO-5290 (Fox et al. 2024; Ashall et al. 2024b). This paper is the second in a series investigating the evolution of SN 2023ixf's panchromatic observations. Here, we provide a detailed identification and analysis of emission lines associated with SN 2023ixf and compare the IR data of SN 2023ixf with those of previous SNe II observed during the Spitzer Space Telescope (*SST*) era and prior.

First, in Section 2 we present a brief overview of previous work on SN 2023ixf. Followed by Section 3, where we describe the panchromatic $0.32 - 30$ μm photometric and spectroscopic observations and data reductions. Then in Section 4, we discuss the evolving panchromatic data of SN 2023ixf and in Section 5 we examine the key spectral features in the full optical to MIR spectrum

of SN 2023ixf. In Section 6, we compare the NIR and MIR spectra of SN 2023ixf to those of other SNe II, enabling us to identify spectral differences. The evolving line velocities of several prominent species are discussed in Section 7. Followed by a discussion on the location of the dust in the ejecta in Section 8. Finally, we present a summary of the results derived from the panchromatic observations of SN 2023ixf in Section 9.

2. PREVIOUS STUDIES ON SN 2023IXF

SN 2023ixf, discovered on 2023 May 19.72 (MJD=60083.73; Itagaki 2023), was rapidly classified as a SN II displaying prominent flash ionization features (Perley & Gal-Yam 2023; Zimmerman et al. 2024). As one of the closest CC-SNe in the last decade, the discovery of SN 2023ixf triggered an unprecedented follow-up campaign across the electromagnetic spectrum ranging from γ-ray to radio, along with multiple multi-messenger searches (e.g., Berger et al. 2023; Bostroem et al. 2023; Chandra et al. 2024; Grefenstette et al. 2023; Hiramatsu et al. 2023; Jacobson-Galán et al. 2023; Sarmah 2024; Singh et al. 2024; Smith et al. 2023; Stritzinger et al. 2023; Teja et al. 2023; Yamanaka et al. 2023; Zimmerman et al. 2024; Guetta et al. 2023; Thwaites et al. 2023; Martí-Devesa et al. 2024; Panjkov et al. 2024; Ravensburg et al. 2024; Van Dyk et al. 2024a; Iwata et al. 2025; Abac et al. 2025; Nayana et al. 2025), including *JWST* observations.

Early-time spectra of SN 2023ixf revealed a blue continuum with prominent narrow ($v \lesssim 300$ km s^{-1}) emission lines from H and ionized He, C, and N, which persisted for several days (Perley & Gal-Yam 2023; Smith et al. 2023; Stritzinger et al. 2023; Vasylyev et al. 2023; Yamanaka et al. 2023; Zimmerman et al. 2024). These features arise from the ejecta interacting with a dense, asymmetric CSM located $\sim (0.5-1) \times 10^{15}$ cm from the progenitor (Bostroem et al. 2023; Jacobson-Galán et al. 2023; Vasylyev et al. 2023; Nayana et al. 2025). The spectra of SN 2023ixf evolved over several months, exhibiting typical SNe II characteristics with a ~ 70 d long hydrogen recombination plateau phase (Zimmerman et al. 2024; Singh et al. 2024; Zheng et al. 2025).

Pre-explosion multi-wavelength imaging at the site of SN 2023ixf indicates a red supergiant progenitor (e.g. Kilpatrick et al. 2023; Jencson et al. 2023; Niu et al. 2023; Pledger & Shara 2023; Soraisam et al. 2023; Ransome et al. 2024). Estimates of the progenitor's mass are bi-modal, with models suggesting either a low-mass progenitor ($M_{\rm ZAMS} = 8-12$ M$_\odot$; Kilpatrick et al. 2023; Pledger & Shara 2023; Van Dyk et al. 2024b; Bersten et al. 2024; Neustadt et al. 2024; Singh et al. 2024; Xiang et al. 2024) or a more massive one ($M_{\rm ZAMS} = 17-22$ M$_\odot$; Jencson et al. 2023; Liu et al. 2023; Niu et al. 2023; Soraisam et al. 2023; Qin et al. 2024). Analysis of nebular-phase spectra did not decidedly confirm a low or high mass progenitor, with mass estimates between $M_{\rm ZAMS}= 12-15$ M$_\odot$ (Ferrari et al. 2024; Folatelli et al. 2025; Kumar et al. 2025; Michel et al. 2025).

Pre-explosion imaging of SN 2023ixf reveals clear evidence of enhanced mass loss in the final years before explosion (Jencson et al. 2023; Soraisam et al. 2023; Flinner et al. 2023; Zhang et al. 2023; Panjkov et al. 2024; Qin et al. 2024; Xiang et al. 2024). While mass-loss rates inferred from imaging were modest ($10^{-6}-10^{-4}$ M$_\odot$ yr^{-1}), early-time light curve and spectral modeling suggests a significantly higher rate ($10^{-3}-10^{-2}$ M$_\odot$ yr^{-1}), implying a major mass-loss episode shortly before explosion (Bostroem et al. 2023; Jacobson-Galán et al. 2023; Teja et al. 2023). Pre-explosion observations from the *SST* show a strong IR signal from the progenitor, consistent with heavy obscuration by dust surrounding the progenitor (Szalai & Van Dyk 2023; Soraisam et al. 2023; Van Dyk et al. 2024b).

The proximity of SN 2023ixf at $\sim 6.9 \pm 0.1$ Mpc (Riess et al. 2022), makes it an ideal candidate for *JWST* follow-up. An initial *JWST* observation of SN 2023ixf was obtained during the plateau phase at +33.6 d post explosion under our project JWST-DD-4722 (Ashall et al. 2023b), and is presented in the first paper of this series (DerKacy et al. 2025, hereafter, Paper I). These observations showed no signs of molecules or dust.

Table 1. Basic observational parameters of SN 2023ixf

Parameter	Value	Source
Right Ascension	$14^h03^m38^s.56$	(1)
Declination	$+54°18'41''.94$	(1)
$T_{\rm exp}$ (MJD)	60082.75	(2)
$V_{\rm max}$ (mag)	~ -18.1	(3, 4, 5)
z	0.0008	(6)
Distance [Mpc]	6.9 ± 0.1	(6)
μ [Mpc]	29.18 ± 0.04	(6)
E(B-V)$_{MW}$ [mag]	0.0077 ± 0.0002	(7)
E(B-V)$_{Host}$ [mag]	0.031 ± 0.012	(8)

References—(1) TNS, (2) Hosseinzadeh et al. (2023), (3) Teja et al. (2023), (4) Jacobson-Galán et al. (2023), (5) Zimmerman et al. (2024), (6) Riess et al. (2022), (7) Schlafly & Finkbeiner (2011), (8) Smith et al. (2023)

3. OBSERVATIONS AND DATA REDUCTIONS

In this section, we describe the *JWST* and ground-based observations, and the data reduction methods. The key properties of SN 2023ixf, such as distance, extinction, and explosion date, adopted throughout this

Figure 1. A stacked three-color image of the host-galaxy spiral arm using the *F770W*, *F1000W*, and *F1500W* MIRI filters from epoch 301.72 d. The location of SN 2023ixf is highlighted by the light blue circle.

work are listed in Table 1. All phases discussed here after are reported in rest-frame days relative to the date of explosion provided in Table 1.

3.1. *JWST MIRI Imaging*

We obtained three epochs of *JWST* MIRI imaging of SN 2023ixf through two of our programs: JWST-GO-3921 (Fox et al. 2024) and JWST-GO-5290 (Ashall et al. 2024b). The first epoch, acquired by JWST-GO-3921 at +301.72 d post-explosion, includes imaging in the *F770W*, *F1000W*, *F1500W*, and *F2100W* filters. The second and third epochs, obtained by JWST-GO-5290 at +600.21 and +719.96 d, use the same instrument with the *F1500W*, *F1800W*, *F2100W*, and *F2500W* filters. A stacked color image from the first epoch is presented in Fig. 1. We perform point spread function (PSF) photometry using a custom Python notebook built on the *WebbPSF*-based `space_phot` package (Perrin et al. 2014)[1]. We select the PSF width to minimize residuals in the fit, accounting for the expected wavelength-dependent broadening. For each dither in which SN 2023ixf is detected, we average the individual flux measurements and estimate the photometric uncertainty from the standard deviation across the dithers. The AB magnitudes and corresponding flux densities (in mJy) for all filters and epochs are summarized in Table 2.

[1] https://github.com/orifox/psf_phot/blob/main/space_phot/MIRI/miri_1028.ipynb

3.2. *JWST Spectroscopy*

We obtained *JWST* spectra of SN 2023ixf on 2024-01-26, 2024-05-26, 2025-01-08, and 2025-05-02 using NIRSpec (Jakobsen et al. 2022; Böker et al. 2023) and MIRI in Low Resolution Spectroscopy mode (MIRI/LRS; Kendrew et al. 2015). We reduced all spectra using the standard NIRSpec fixed-slit and MIRI LRS-slit Jupyter notebooks (Law et al. 2025), with version 1.18.0 of the *JWST* calibration pipeline (Bushouse et al. 2022), *JWST* Build version 11.3, and Calibration Reference Data System file `jwst_1364.pmap`.

3.2.1. *NIRSpec*

The NIRSpec observations used the F170LP/G235M and F290LP/G395M filter/grating combinations, covering the 1.66–3.07 μm and 2.87–5.10 μm ranges, respectively. The observations employed the S400A1 subarray and a 3-Point-Nod dither pattern. Exposure times were increased over time to account for the fading SN flux, ensuring a high enough signal-to-noise ratio (SNR) to

Table 2. Observation log of *JWST* photometric imaging taken through our program JWST-GO-3921 (Fox et al. 2024) at + 301.72 d and our program JWST-GO-5290 (Ashall et al. 2024b) at + 600.21 and + 719.96 d. The epochs are given in days from explosion. Magnitudes and fluxes are not corrected for extinction

	Epoch	*F770W*	*F1000W*	*F1500W*	*F1800W*	*F2100W*	*F2500W*
AB Mag. [mag]	301.72	14.803 ± 0.013	14.51 ± 0.008	15.023 ± 0.005	-	15.346 ± 0.002	-
	600.21	-	-	15.214 ± 0.001	15.180 ± 0.002	15.274 ± 0.002	15.351 ± 0.004
	719.96	-	-	15.269 ± 0.001	14.601 ± 0.001	15.283 ± 0.003	15.348 ± 0.004
Flux Density [mJy]	301.72	4.353 ± 0.052	5.702 ± 0.042	3.555 ± 0.016	-	2.64 ± 0.005	-
	600.21	-	-	2.983 ± 0.003	3.076 ± 0.005	2.822 ± 0.004	2.627 ± 0.01
	719.96	-	-	2.834 ± 0.003	5.222 ± 0.002	2.798 ± 0.007	2.635 ± 0.01

trace the evolution of the CO first overtone, fundamental band, and other spectral features. Full details of the NIRSpec configuration are provided in Appendix A.

We modified the standard reduction parameters to include a scaling factor in the `outlier_detection` step during stage 3 spectroscopic processing. This scale value varies between 0 and 1.2 to minimize noise spikes, caused by bad pixels when combining the three dithers, while preserving the source flux. All reduction stages; stage 1 detector processing, stage 2 image processing, stage 2 spectroscopic processing, and stage 3 spectroscopic processing, were run on uncalibrated NIRSpec images downloaded from the Barbara A. Mikulski Archive for Space Telescopes (MAST[2]).

3.2.2. *MIRI-LRS*

The MIRI observations utilized the LRS mode, covering a wavelength range of $\sim$ 5–14 μm (Kendrew et al. 2015). All epochs were taken using the full subarray, the FASTR1 readout pattern, and the Along-Slit-Nod dither pattern. Exposure times were increased to account for the declining flux of SN 2023ixf. Details on the exposure times and readout settings for each epoch are provided in Appendix A. We use the standard reduction parameters to run all processing stages on the uncalibrated MIRI-LRS images downloaded from MAST.

3.3. *Ground-Based Spectroscopy*

The ground based optical and NIR observations were obtained as close to contemporaneous with the *JWST* observations as possible to ensure no significant evolution of the emission features between the observations. Details on the optical and ground-based NIR observations, and the full spectra obtained are presented in Appendix A, and Figures A1 and A2 respectively.

3.3.1. *Optical*

Optical spectra were obtained at similar epochs to the *JWST* spectral observations using the Optical System for Imaging and low-Intermediate-Resolution Integrated Spectroscopy (OSIRIS+) on the 10.4-m Gran Telescopio Canarias (GTC; Alvarez et al. 1998). We reduce the GTC data using standard procedures, including bias subtraction, flat-fielding of the two-dimensional images, wavelength calibration of the extracted spectrum from arc lamp exposures, and the removal and correction of telluric features and cosmic rays. Multiple exposures were obtained in the R1000B and R1000R filters and median-combined to increase the signal-to-noise of the optical spectra. An additional optical spectrum was obtained using the 10-m Keck-I telescope with the Low-Resolution Imaging Spectrometer (LRIS; Oke et al. 1995; McCarthy et al. 1998; Rockosi et al. 2010) to complement the +713-d *JWST* spectra. The LRIS observations used the 600/4000 grism on the blue side and the 400/8500 grating on the red side. Multiple images were obtained with exposure times of 1800 s and 900 s for the blue and red arms. We reduce the individual arms separately using the automated spectroscopic reduction code `Pypeit`[3], version 1.17.3.

Optical spectra, covering 72 − 279 d, were taken on the University of Hawai'i 88-inch telescope (UH88) located on Maunakea using the SuperNova Integral Field Spectrograph (SNIFS: Aldering et al. 2002; Lantz et al. 2004) through the Spectroscopic Classification of Astronomical Transients (SCAT; Tucker et al. 2022) survey, as well as on the Intermediate Dispersion Spectrograph (IDS[4]) mounted on the Isaac Newton Telescope (INT). We reduce the SNIFS spectra using the procedure detailed in Tucker et al. (2022), and the IDS, spectra via the standard reduction pipeline (Müller Bravo 2023).

[2] https://mast.stsci.edu/portal/Mashup/Clients/Mast/Portal.html

[3] https://pypeit.readthedocs.io/en/1.17.3/index.html

[4] https://www.ing.iac.es/Astronomy/telescopes/int/

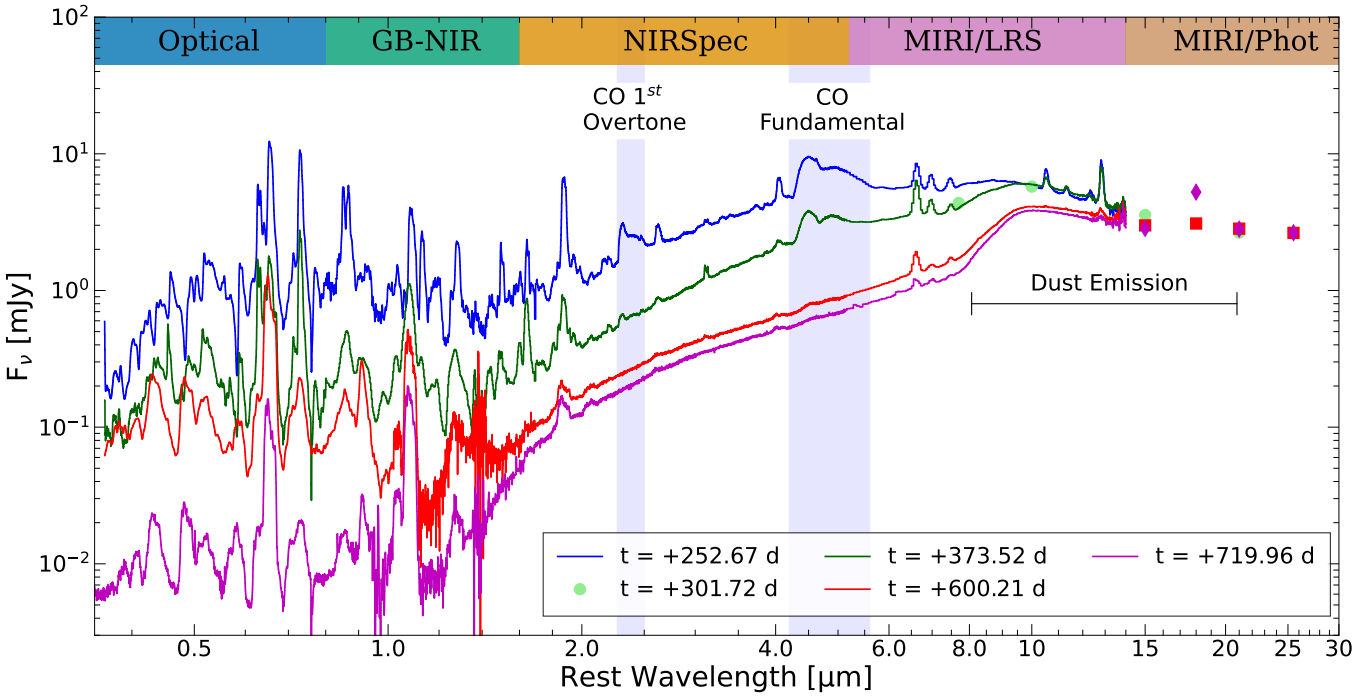

Figure 2. The evolution of the SED covering $0.32 - 14.0$ μm of SN 2023ixf from +252.67 d to +719.96 d post explosion. Photometry is shown by the colored symbols, at +301.72 d, +600.21 d, and +719.96 d. The data have been corrected for extinction and are presented in the rest frame. The SED's are dominated by a large number of emission lines that decline in strength as SN 2023ixf evolves. CO molecule and dust features are highlighted. In addition, there is a strong IR excess that grows in strength relative to the SN flux at late times.

3.3.2. *Near Infrared*

NIR spectra covering $\sim 0.7 - 2.5$ μm were obtained by the Hawai'i Infrared Supernova Study (Medler et al. 2025) using SpeX (Rayner et al. 2003) on the 3.0-m NASA Infrared Telescope Facility (IRTF) and the Near-Infrared Echellette Spectrometer (NIRES; Wilson et al. 2004) on the 10-m Keck-II telescope.

The IRTF spectra were taken in ShortXD mode, with a slit size of $0.8'' \times 15''$ using ABBA dithering. We reduce these observations with the `Spextool` software package (Cushing et al. 2004) applying telluric corrections that use an AV0 star that was at a similar airmass to SN 2023ixf. More details on the reduction procedure can be found in Medler et al. (2025); Hoogendam et al. (2025a) and Hoogendam et al. (2025b).

The NIRES spectra were also taken using ABBA dither patterns with 300s individual exposure times. We reduce these Keck-II/NIRES observations in a similar manner to the IRTF/SpeX observations, using the Keck-II/NIRES version of the `Spextool` package (for more information, see Medler et al. 2025).

An additional spectrum was obtained with GTC using the Espectrógrafo Multiobjeto Infra-Rojo spectroscope (EMIR; Garzón et al. 2022). We reduce the EMIR observations with our own pipeline based on PyEmir (Pascual et al. 2010; Cardiel et al. 2019; Pascual et al. 2019).

4. SPECTRAL ENERGY DISTRIBUTION

Figure 2 presents the $0.32 - 30.0$ μm spectral energy distribution (SED) of SN 2023ixf, spanning from +252.67 to +719.96 d. The SED's remain relatively flat between 0.32 and 1.2 μm and are dominated by forbidden line transitions, which evolve in both strength and velocity as different regions of the ejecta become exposed.

During the first two epochs, the SEDs show strong emission from the first overtone and fundamental ro-vibrational bands of CO. These emission features weaken substantially by +600.21 d indicating a decrease in the temperature of the CO region to below 1000 K (Liljegren et al. 2020). Future papers in this series will discuss the modeling of the CO features and derived CO properties in SN 2023ixf.

Across the IR regime above 1.5 μm, the flux continuum rises to a peak at ~ 10.0 μm in the +252.67 d spectrum indicating the presence of warm dust. As SN 2023ixf evolves the IR continuum flux declines in strength alongside the optical, suggesting that the dust mass does not significantly increase during these epochs. By +600.21 d, the 10.0 μm peak dominates the MIR

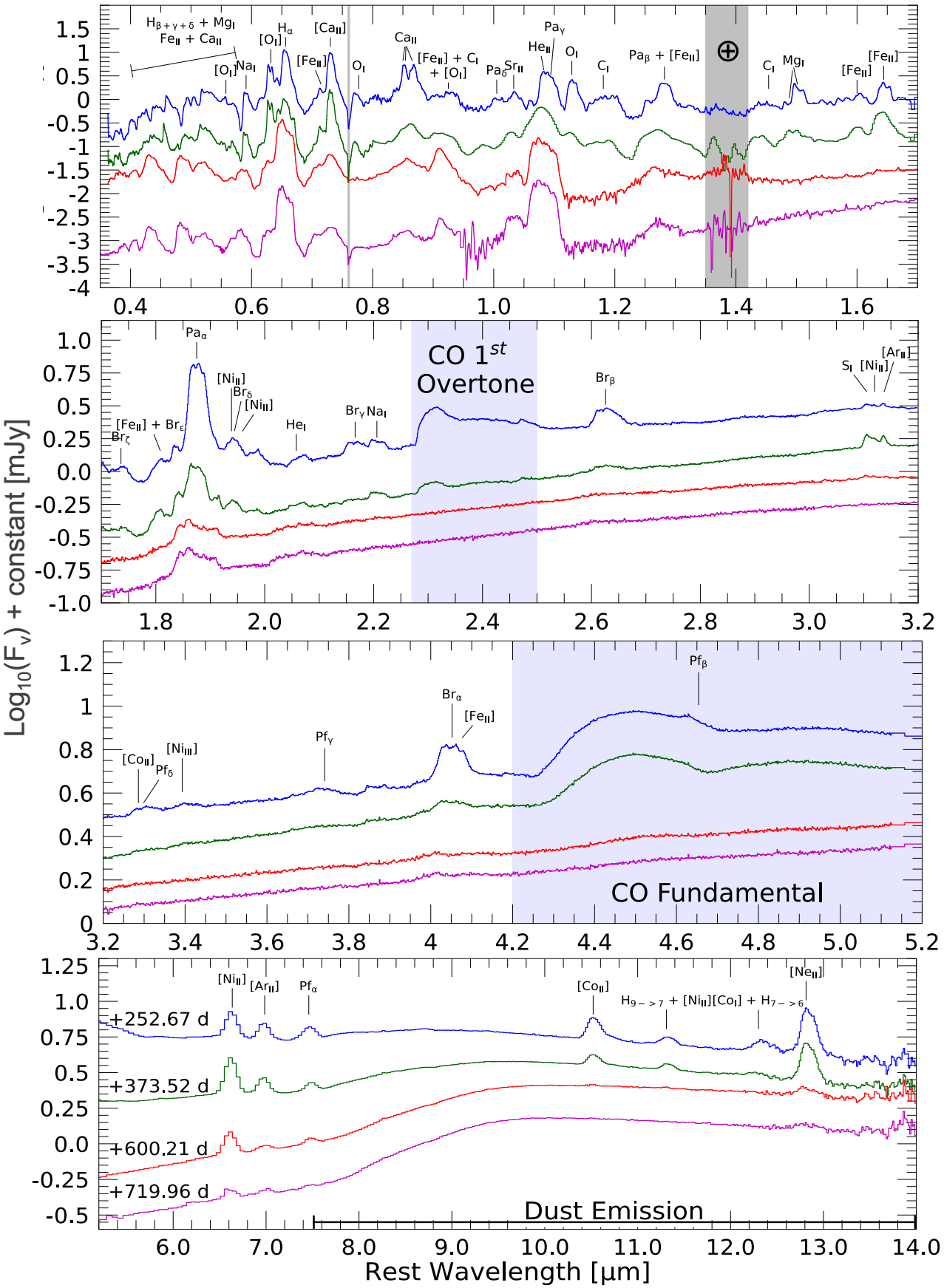

Figure 3. Lines identified within the ground based optical and NIR (top row), *JWST* NIRSpec G235M/F170LP (second row), G395/F290LP (third row) and MIRI (fourth row) spectra of SN 2023ixf at ∼ 250 d (blue), ∼ 373 d (green), ∼ 600 d (red), and ∼ 720 d (purple) post explosion. The spectra have been vertically shifted for clarity. The CO 1st overtone, and CO fundamental band are shown by the shaded blue regions. The full list of identified lines is given in Tables 3 and 4.

spectrum over any emission feature, while a secondary peak at 18.0 μm emerges by +719.96 d. These two MIR features suggest a significant contribution to the flux from Si-rich dust at these later epochs (Chiar & Tielens 2006; van Breemen et al. 2011; Shahbandeh et al. 2023), see section 8 for further discussion.

5. IDENTIFICATIONS OF EMISSION LINES

The identification of spectral features in the late-time spectra of SN 2023ixf provides critical insight into the structure and composition of the ejecta. The dominant features in the +252.67 optical and ground-based NIR SED's of SN 2023ixf include several strong H emission lines, primarily from low-level transitions, as well as prominent O, Mg, and Ca features, as shown in the top panel of Fig. 3. Iron-group elements such as Fe, Ni, and Co, along with other α elements, dominate the emission features in the *JWST* NIR and MIR regions. As SN 2023ixf evolves, the strength of all emission lines gradually declines as the SN component of the SED fades. The MIR emission lines become increasingly suppressed due to the growing contribution from the IR excess which dominates the SED's, particularly at $t \geq +600$ d.

Below, we highlight the strongest lines of key elemental species identified in the nebular-phase spectra from both ground-based and *JWST* observations. To support the analysis, we compile spectral lines from previous studies of late-time SNe II spanning the optical, NIR, and MIR regimes (e.g., Jerkstrand et al. 2012; Davis et al. 2019; Shahbandeh et al. 2022). The identified spectral lines appear in Tables 3 and 4.

5.1. *Hydrogen*

Throughout the evolution of SN 2023ixf, we identify strong hydrogen emission lines from multiple transition series across the optical to MIR spectrum, with several lines displaying strong blending. The observed H lines include: Balmer series ($n = 2$): Hα 0.6563 μm, Hβ 0.4861 μm, Hγ 0.4340 μm, and Hδ 0.4102 μm; Paschen series ($n = 3$): Paα 1.875 μm, Paβ 1.282 μm, Paγ 1.094 μm, and Paδ 1.005 μm; Brackett series ($n = 4$): Brα 4.051 μm, Brβ 2.626 μm, Brγ 2.166 μm, Brδ 1.944 μm, and Brε 1.817 μm; Pfund series ($n = 5$): Pfα 7.460 μm, Pfβ 4.654 μm, Pfγ 3.741 μm, and Pfδ 3.297 μm; Humphreys series ($n = 6$): Huα 12.37 μm and Huβ 7.503 μm. We also identify potential emission lines from higher-order transitions, such as $H_{n=9\rightarrow7}$ 11.309 μm and $H_{n=11\rightarrow8}$ 12.372 μm.

The emission peaks from the higher-order Balmer series are absent between +252.67 − +373.52 d as these lines lie within absorption features dominated by heavy elements, particularly Fe, but emerge between +373.52 d and +600.21 d. The α through ε transitions of the Paschen, Brackett, Pfund, and Humphreys series are detected in the +252.67 and +373.53 d spectra. However, at later epochs (+600.21 and +719.96 d), the higher-order transitions, especially the δ and ε lines, become too weak to detect.

The hydrogen lines evolve from the standard P-Cygni profile observed at earlier epochs (Paper I) and exhibit three distinct components centered around the rest-frame emission wavelength. The first is a strongly blueshifted peak; the second is a weak, narrow peak located slightly redward of the rest wavelength; and the third is a broad red shoulder. We discuss the origin of these features in detail in Section 7.

5.2. *Helium*

In the optical, He lines are difficult to identify due to significant line blending and contamination from other emission features, particularly those from H, Fe, and Na. However, we tentatively identify several weak features commonly associated with He, including He I 0.5876 μm, He I 0.6678 μm, and He I 0.7065 μm. In the NIR we identify the strong He I 1.083 μm and He I 2.058 μm.

5.3. *Carbon*

We identify multiple carbon features, all from neutral C, at C I 0.94 μm, 1.176 μm, 1.181 μm, and 1.454 μm. While the C I 0.94 μm line blends with nearby O and Fe lines, the other NIR lines are either isolated or blended only with adjacent C lines. Spectral models of other late-time SNe II (Jerkstrand et al. 2012) also identify these features which, together with the prominent CO emission observed in the spectra, supporting the identification of C in SN 2023ixf.

5.4. *Oxygen*

Throughout the optical and NIR spectra, we identify several emission features associated with oxygen. The strongest O lines in the spectra of SN 2023ixf are the forbidden optical doublet [O I] 0.6300 and 0.6363 μm. In addition to this doublet, we detect several other forbidden and permitted O lines, including [O I] 0.5577 μm, the O I 0.777 μm triplet, [O I] 0.9266 μm, and O I 1.1290 μm. The strength of all O features declines over time, with the NIR lines becoming undetectable between the +373.52 and +600.21 d spectra. We discuss the evolution of the [O I] 0.6300 and 0.6363 μm feature in detail in Section 7.

5.5. *Neon*

A prominent Ne line, associated with the [Ne II] 12.813 μm transition, appears in the nebu-

lar phase MIRI-LRS spectra of SN 2023ixf. No other Ne II lines or other excitation states of Ne are identified in the spectra of SN 2023ixf. This line has also been detected in several MIR observations of other SNe II (Kotak et al. 2006; Meikle et al. 2007, 2011).

5.6. *Argon*

We identify a strong emission feature associated with the [Ar II] 6.985 μm line. Other lines of Ar, such as [Ar III] 8.991 μm, are not detected in the spectrum, which may indicate that a significant fraction of both noble gases, including Ar and Ne, remain in a neutral state. A similar phenomenon may have also been present in SN 2005af (Kotak et al. 2006).

5.7. *Calcium*

The spectra of SN 2023ixf show multiple Ca lines from both forbidden and permitted transitions. These include the permitted Ca II NIR triplet at 0.8498, 0.8542, and 0.8662 μm, the Ca II H&K lines at 0.3934 and 0.3969 μm, and the forbidden [Ca II] 0.7292 and 0.7324 μm lines. As SN 2023ixf evolves, the permitted Ca lines decrease in strength, while the forbidden [Ca II] lines grow more prominent relative to the continuum, consistent with a declining ejecta density.

5.8. *Iron*

Strong Fe lines appear throughout the late-time optical-MIR spectra of SN 2023ixf. A blend of several Fe II lines are located between $\sim 0.32 - 0.5$ μm, including Fe II 0.4352 μm, Fe II 0.4924 μm, Fe II 0.5018 μm, and Fe II 0.5169 μm. Additional forbidden and allowed Fe lines are scattered throughout the optical and IR regimes, including [Fe II] 0.7155 μm, [Fe II] 1.279 μm, [Fe II] 1.321 μm, Fe II 1.644 μm, [Fe II] 1.809 μm, Fe II 1.939 μm, Fe II 3.108 μm, Fe II 3.137 μm, and [Fe II] 4.075 μm. We also tentatively identify several weak emission features associated with neutral Fe throughout the spectra of SN 2023ixf, including Fe I 0.5270 μm, Fe I 0.5328 μm, Fe I 0.5587 μm, Fe I 0.7187 μm, and Fe I 1.980 μm.

5.9. *Cobalt*

We identify several forbidden Co lines in the spectra of SN 2023ixf, including [Co II] 1.019 μm, [Co II] 3.286 μm, [Co II] 10.521 μm, and [Co I] 12.255 μm. We also observe weak features associated with the second ionization state of Co, such as [Co III] 11.886 μm and [Co III] 13.813 μm. However, these features are either very weak relative to the continuum or located near the edge of the instrument's spectral range where throughput decreases, obfuscating their exact strength and evolution.

5.10. *Nickel*

In addition to the forbidden Co lines, we identify several forbidden lines from neutral and first ionization state Ni. These include: [Ni I] 3.120 μm, [Ni I] 11.308 μm, [Ni II] 1.939 μm, [Ni II] 1.958 μm, [Ni II] 6.636 μm, and [Ni II] 10.682 μm.

5.11. *Other Species*

We also detect several emission features associated with other elements including: Na (Na I 0.5896 μm, Na I 2.206 μm), Mg (Mg I 0.3832 μm, Mg I 0.457 μm, Mg I 0.518 μm, Mg I 0.517 μm, Mg I 1.488 μm, and Mg I 1.502 μm), Si (Si I 1.203 μm, Si I 1.033 μm, Si I 1.066 μm, [Si I] 1.606 μm, and [Si I] 1.645 μm), S (S I 3.107 μm), Ba (Ba II 0.6142 μm) and Sr (Sr II 1.004 μm, Sr II 1.033 μm, and Sr II 1.092 μm). These lines blend with other emission features, forming shoulders or broad peaks centered between the blended lines.

5.12. *Molecules*

Several molecular emission features are observed in the NIR/MIR spectra of SN 2023ixf which were not present in the initial *JWST* data (Paper I). Here, we examine the evolution of molecules in SN 2023ixf as it transitions from the SN-dominated phase to the dust-dominated phase, while deferring the spectroscopic modeling of SN 2023ixf's molecular features to a future paper in the series.

Two strong features appear in the spectra of SN 2023ixf corresponding to the first overtone and fundamental ro-vibrational bands of CO. Ground-based NIR observations show the emergence of the CO first overtone between +81 d (Li et al. 2025) and +200 d (Park et al. 2025). In the *JWST* observations, these features dominate the NIR spectrum of SN 2023ixf from +252.67 to +373.13 d, before fading over the following $\sim$ 230 d, see the CO regions in Fig. 2. By +600.21 d, the CO first overtone completely fades below the continuum level. However, the CO fundamental band remains visible even at +717.13 d, where the broad $\nu = 1 \rightarrow 0$ band head is still detectable above the continuum flux.

Throughout the evolution of SN 2023ixf, both the CO first overtone and fundamental possess distinct broad R- and P-branch emission features, in contrast to the spiky nature of the CO features commonly observed in young stellar objects (e.g. Ilee et al. 2018; Fedriani et al. 2020). These broad shapes arise from the high ejecta velocity blending the higher order CO transitions into the π_0 and π_1 transitions.

Emission features in the region between $\sim 7.5-9.5$ μm are typically associated with the SiO fundamental band

Table 3. Identified nebular phase spectral lines present in the optical and ground-based NIR spectra

Ion	Wavelength [μm]	Ion	Wavelength [μm]
Optical spectrum, 0.35 - 1.0 μm			
Mg I	0.38	Fe I	0.5587
Ca II	0.3934	Na I	0.5896
Ca II	0.3969	Ba II	0.6142
Hδ	0.410.2	[O I]	0.6300
Hγ	0.4340	[O I]	0.6363
Fe II	0.4352	α	0.6563
Mg I]	0.457	[Fe II]	0.7155
Hβ	0.4861	Fe I	0.7187
Fe II	0.4924	[Ca II]	0.7292
Fe II	0.5018	[Ca II]	0.7324
Fe II	0.5169	O I	0.777
Mg I	0.517	Ca II	0.8498
Mg I	0.518	Ca II	0.8542
Mg I	0.518	Ca II	0.8662
Fe I	0.5270	[O I]	0.9266
Fe I	0.5328	C I	0.94
[O I]	0.5577		
GB-NIR spectrum, 1.0 - 1.6 μm			
Sr II	1.004	Si I	1.203
Paδ	1.005	[Fe II]	1.279
[Co II]	1.019	Paβ	1.282
Si I	1.033	[Fe II]	1.321
Sr II	1.033	C I	1.454
Si I	1.066	Mg I	1.488
He I	1.0830	Mg I	1.502
Sr II	1.092	[Si I]	1.606
Paγ	1.094	Fe II	1.644
O I	1.1290	[Si I]	1.645
C I	1.181		

Table 4. Identified nebular phase spectral lines present in the *JWST* NIR and MIR spectra

Ion	Wavelength [μm]	Ion	Wavelength [μm]
NIRSpec spectrum, 1.6 - 5.2 μm			
He I	1.7002	Brβ	2.626
C I	1.176	S I	3.107
[Fe II]	1.809	Fe II	3.108
Brε	1.817	[Ni I]	3.120
Paα	1.875	Ar II	3.137
Fe II	1.939	Fe II	3.137
[Ni II]	1.939	Pfδ	3.297
Brδ	1.944	[Co II]	3.286
[Ni II]	1.958	Pfγ	3.741
Fe I	1.980	Brα	4.051
He I	2.0581	[Fe II]	4.075
Brγ	2.166	Pfβ	4.654
Na I	2.206		
MIRI spectrum, 5.2 - 14 μm			
[Ni II]	6.636	$H_{n=9\rightarrow7}$	11.309
[Ar II]	6.985	[Co III]	11.886
Pfα	7.460	[Co I]	12.255
Huβ	7.503	Huα	12.37
[Co II]	10.521	$H_{n=11\rightarrow8}$	12.372
[Ni II]	10.682	[Ne II]	12.813
[Ni I]	11.308	[Co III]	13.813

(Liu & Dalgarno 1994; Kotak et al. 2006). However, this region in SN 2023ixf does not show the strong emission features expected from SiO vibrational bands at any epoch, instead possessing a rising IR continuum, see Fig. 2.

6. SPECTRAL COMPARISON

To evaluate the uniqueness of SN 2023ixf's infrared spectral features relative to other SNe II, we compare the NIR and MIR spectroscopic observations of SN 2023ixf and several other objects. This comparison reveals both shared and unique features, constraining the structural diversity of these events. As SN 2023ixf evolves, the IR continuum grows stronger and the SN flux fades drowning out the features from atomic lines. To accurately contrast SN 2023ixf with the other SNe II, we remove the IR continuum by fitting a blackbody at each epoch. A single blackbody, while not physically representative of the underlying physics, works well to capture the shape of the continuum at earlier times, while at later times the dust becomes optically thin preventing a single blackbody from capturing the full IR continuum shape.

6.1. *NIR Comparison*

Historically, observations of SNe II in the NIR at late times ($t > 200$ d) have been sparse because of their low luminosities and the lack of telescopes capable of observing these wavelengths. Until recently (Shahbandeh et al. 2024, Paper I, Baron et al. 2025, Mera et al. 2025), SN 1987A was the only SN II with NIR spectroscopic data between $2.5 - 5$ μm, obtained from the Kuiper Airborne Observatory (Wooden et al. 1993). This limited sample prevents robust conclusions regarding the

uniqueness of the NIR emission lines and molecular features in SN 2023ixf, especially considering its dusty progenitor, which differs drastically from the blue supergiant progenitor of SN 1987A (Chevalier & Fransson 1987; Woosley et al. 1988; Arnett et al. 1989; Podsiadlowski 1992). The comparison of the late-time NIR spectra of SN 1987A and SN 2023ixf is shown in the left-hand panel of Fig. 4.

Even more than a year after explosion, both SN 1987A and SN 2023ixf exhibit several strong H lines throughout the NIR region. The strongest of these lines are the Paα, Brα, and Brβ transitions. Additional weaker spectral features associated with Brγ and Pfβ also appear in both datasets, although they are less prominent in SN 2023ixf due to the strong contribution from the warm dust. A feature located at ~ 3.2 μm, identified as the [Ni I] 3.120 μm line in the SN 1987A spectrum (Wooden et al. 1993), is present in the +415 d spectrum of SN 1987A and in the +253 to +600 d spectra of SN 2023ixf. While it appears as a single, blended emission feature with a blue shoulder in SN 1987A, the same feature in SN 2023ixf is resolved into a double-peaked structure. However, the difference in shape between the two SNe is likely due to the higher resolution of the *JWST* spectra.

In contrast to SN 2023ixf, SN 1987A does not exhibit a rising continuum; instead displaying a relatively flat flux across the NIR region. At >1 year post-explosion, after removing the infrared excess in SN 2023ixf, both SNe display similar CO fundamental features at ~ 5 μm and a weak first overtone feature. Interestingly, the ratio of the CO fundamental peak to the Brα line is much higher in SN 2023ixf than in SN 1987A and a more prominent Pfβ is also observed in SN 1987A, see Fig. 4. This difference is particularly pronounced at later times, where the CO fundamental in SN 2023ixf is dominant over the Brα emission, while in SN 1987A, both features are of similar intensity. The disparity in CO and Brα intensities may suggest that SN 2023ixf produced significantly more CO than SN 1987A at these epochs. If this is the case, and if we assume that the majority of C and O is bound in CO, then SN 2023ixf would have a larger C/O core than SN 1987A and thus a larger potential initial progenitor mass. However, given the unique status of SN 1987A's progenitor (Woosley et al. 1988; Arnett et al. 1989), a large C/O core in SN 2023ixf is only tentatively suggested.

6.2. *MIR Comparison*

In contrast to the NIR, several SNe II beyond just SN 1987A have been observed at $\lambda > 5$ μm thanks to Spitzer-era programs, including SN 2004dj (Szalai et al. 2011), SN 2004et (Kotak et al. 2009), and SN 2005af (Kotak et al. 2006). The comparison with SN 2023ixf is shown in the right hand panel of Fig. 4. The emission lines of SN 2023ixf appear weaker than those in other SNe II, due to the strong IR excess that enhances the continuum, reducing the relative line strength especially at longer wavelengths. Once the continuum is subtracted the line strengths of SN 2023ixf become comparable to the other SNe.

Strong emission features are consistently found across all SNe. These features are associated with Co and Ni lines as well as the α-elements Ne and Ar. In addition, SN 2023ixf lacks a strong emission of SiO between $7-9.5$ μm unlike other SNe, especially SN 1987A. The line strength ratios of the [Ni II] 6.636 μm, [Ar II] 6.985 μm, and Pfα 7.460 μm features of SN 2023ixf are consistent with the other SNe with the exception of SN 2004dj, which possesses a weaker [Ar II] 6.985 μm feature.

The [Ne II] 12.813 μm feature is significantly stronger in SN 2023ixf at all phases relative to the other SNe. While it has been suggested that this line can be powered by interaction (Tinyanont et al. 2025), we do not see signatures of interactions such as narrow lines or flat-tops in this line suggesting the [Ne II] 12.813 μm originates from within the ejecta. The presence of a strong [Ne II] 12.813 μm feature indicates that the progenitor of SN 2023ixf possessed a relatively large pre-explosion Ne mass (Jerkstrand et al. 2012), which has been associated with a higher progenitor mass (Woosley & Weaver 1995; Woosley et al. 2002). Nebular phase modeling of SN 2004et showed that the [Ni II] 12.729 μm line becomes significantly stronger as the progenitor mass increases (Jerkstrand et al. 2012). Thus, the strong [Ne II] 12.813 μm line observed in SN 2023ixf suggests a relatively high mass progenitor, potentially larger than the 15 $M_\odot$ progenitor of SN 2004et (Jerkstrand et al. 2012).

The most notable difference between SN 2023ixf and other SNe in the MIR is its exceptionally strong infrared continuum, with NEOWISE 3.4 and 4.6 μm photometry identifying SN 2023ixf as one of the brightest SN II observed in the MIR (Van Dyk et al. 2024a). This strong infrared continuum dominates the spectra of SN 2023ixf over any other emission feature and is significantly stronger than in any other SN II. SN 2023ixf's infrared excess emerges prior to +252.67 d, several hundred days earlier than the other SNe shown in Fig. 4, e.g. SN 2004et developed a strong IR excess after +400 d (Kotak et al. 2006, 2009). The strong IR excess is solely observed in the later epochs, $t \geq +250$ d (Paper I), suggesting that a large amount of dust, either pre-existing or freshly formed, is present. While comprehensive mod-

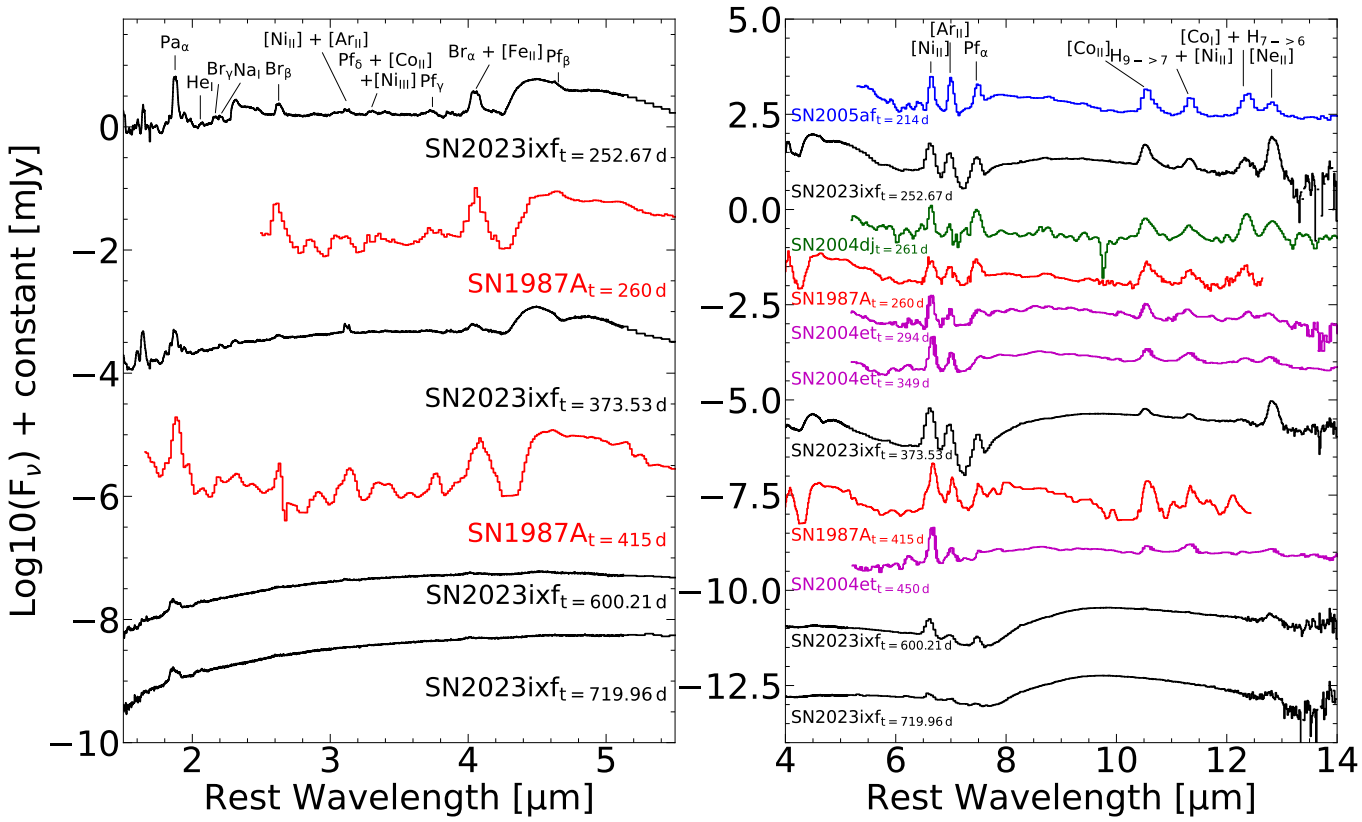

Figure 4. Spectral comparison of SN 2023ixf with several SNe II observed at infrared wavelengths. All spectra have been corrected for redshift and extinction. To aid in comparison, the spectra of SN 2023ixf are continuum subtracted with blackbody functions of 850 K, 550 K, 360 K, and 300 K from the +252.67, +373.52, +600.21, and +719.96 d data, respectively. Left: Comparison of the NIR spectra, between $1.5-5.5$ μm, of SN 1987A and SN 2023ixf. Right: Comparison of the SN 2023ixf MIRI spectra with SN 1987A (Wooden et al. 1993), SN 2004dj Szalai et al. (2011), SN 2004et (Kotak et al. 2009), and SN 2005af (Kotak et al. 2006). Both SN 1987A and SN 2004et were digitized from Wooden et al. (1993) and Kotak et al. (2009), respectively.

eling of the dust component is left for future papers in this series, we discuss the origins of the infrared excess in Section 8.

7. LINE VELOCITIES

The shapes of nebular emission lines are known to encode important information about the physics and evolution of the explosion. Additionally, the shape of spectral line profiles offer a powerful diagnostic for identifying signatures of newly formed dust.

7.1. *Hydrogen Line Diversity*

The H profiles in late time spectra of SNe II have often been used as a key identifier of an asymmetric explosion (Leonard et al. 2002; Utrobin & Chugai 2009) or the formation of dust within the ejecta (Sahu et al. 2006; Kotak et al. 2009; Maguire et al. 2010). Newly formed dust attenuates the flux from the receding side of the SN, resulting in a suppression of the redshifted flux and a slightly blueshifted asymmetrical emission peak. This was first identified in SN 1987A (Lucy et al. 1989a) but has since been observed in multiple SNe (Lucy et al. 1989a; Kotak et al. 2009; Maguire et al. 2010; Stritzinger et al. 2012; Inserra et al. 2011; Smith et al. 2012; Gall et al. 2014). Many H lines are clearly present throughout the evolution of SN 2023ixf and the evolution of the α, β, and γ H transitions from the Balmer to Humphreys series is shown in Fig. 5.

Several of the H features seen in the +252.67 d spectrum display a split three-peaked central profile, e.g. the Hα, Paα, Pa β, Brα, Brβ, and Brγ, see Fig. 5. The three peaks correspond to peak shifts of $-1,100$ km s^{-1}, 600 km s^{-1}, and $2,200$ km s^{-1}, identified as the blue, green and red dashed vertical lines in Fig. 5, respectively. These multiple peaks are not always observed in the higher order transitions, either due to weak line strengths, e.g. Pa γ or blending with emission features from other atomic species or molecules, e.g. Hβ and Pfβ.

The multi-peaked emission features are also visible at +600.21 and +719.96 d although the blueshifted peak has shifted more blue-ward to $\sim -2,500$ km s^{-1}, as seen

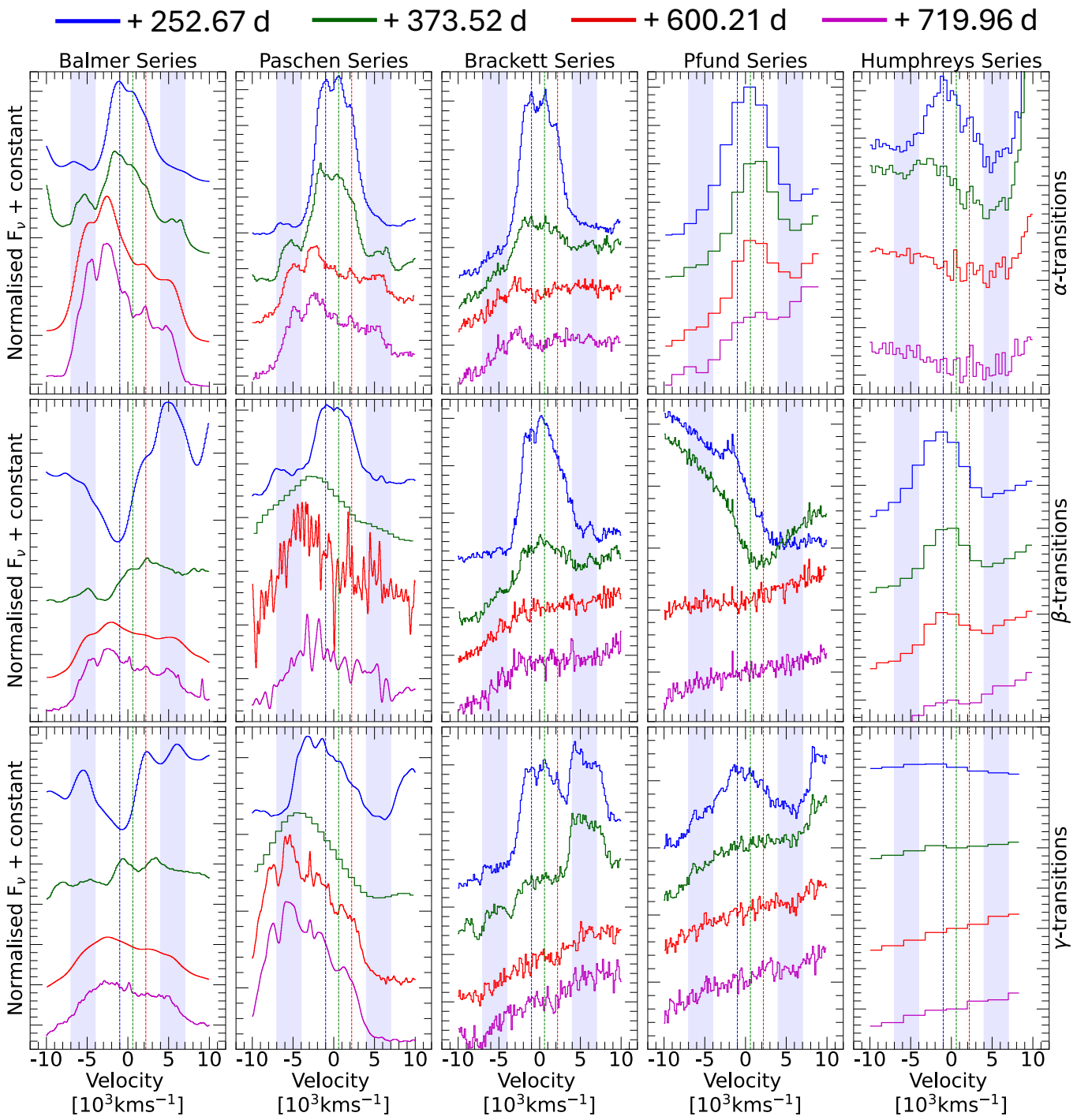

Figure 5. Evolution of the α (top), β (middle), and γ (bottom) transitions of the different hydrogen series located between $0.32 - 14.0$ μm at +252.67 (blue), +373.52 (green), +600.21 (red), and 719.96 d (purple). Several of the isolated hydrogen emission lines, especially the α transitions, show a triple-peaked profile consisting of a blueshifted peak ($-1,100$ km s^{-1}), a slightly redshifted peak (+500 km s^{-1}), and a strongly redshifted shoulder ($+2,200$ km s^{-1}), shown by the vertical dashed blue, green and red lines, respectively. Additional high velocity components, the shaded blue regions, emerge between +252.67 and +372.53 d located between $\pm 4,000 - 8,000$ km s^{-1}.

in the Hα and Paα profiles in the top row of Fig. 5. A similar time-evolving shift is not seen in the two redward peaks. At these later epochs, line blending from other emission features is not significant, hence these peaks are visible in the higher order transitions, see the bottom two spectra of the Hβ and Hγ plots of Fig. 5. The origin of the three shifted Hα peaks in SN 2023ixf has been associated with strong clumping within ejecta and the surrounding swept-up CSM (e.g., Singh et al. 2024; Ferrari et al. 2024; Kumar et al. 2025).

In addition to the evolving multi-peak central emission feature, many of the H profiles exhibit two high-velocity features in the wings of the spectra. These features are boxy in shape and located at between $\pm 4,000 - 8,000$ km s^{-1}, and are shown by the highlighted blue regions in Fig. 5. These structures are most clearly observed in the Hα and Paα transitions.

The distinct high-velocity hydrogen features could be produced by the interaction of a fast-moving, asymmetric shock-front with a low density CSM. While the central triple-peaked features can be explained by a slower moving shock-front interacting with dense equatorial CSM (Singh et al. 2024; Kumar et al. 2025). These complex structure can significantly influence both the molecule and dust formation rates.

7.2. *Hydrogen α-series Evolution*

The study of the α-series transitions, as the strongest transitions in each H-series, allows us to understand properties of the bulk of the H-envelope.

7.2.1. *Hα Evolution*

Examining individual features with high cadence data may be able to provide additional insight into the physics of the explosion which may be missed with sparsely sampled observations. The evolution of the Hα feature between 70 and 720 d is shown in Fig. 6, with the full optical spectra shown in Appendix A.

Prior to +72.16 d the Hα emission feature evolved from a sharp narrow flash ionization emission line (Zimmerman et al. 2024; Jacobson-Galán et al. 2023) to a mostly smooth broad P-Cygni like emission profile (Singh et al. 2024; Zheng et al. 2025; Paper I). The temporal evolution of Hα in Fig. 6, reveals a smooth broad emission peak with an initial blueshift of ~ -1000 km s^{-1} at +72.16 d that declines to rest velocity by +86.44 d as the ejecta becomes optically thin (Anderson et al. 2014), which is accompanied by a decline in FWHM from $8,000 \pm 300$ to $5,900 \pm 300$ km s^{-1}.

Over the ~ 140 days between +86.44 and +212.72 d, the three peaks discussed in Section 7.1 emerge within the Hα profile. These three peaks have velocities of $\sim -1,100$ km s^{-1}, ~ 600 km s^{-1}, and $\sim 2,200$ km s^{-1},

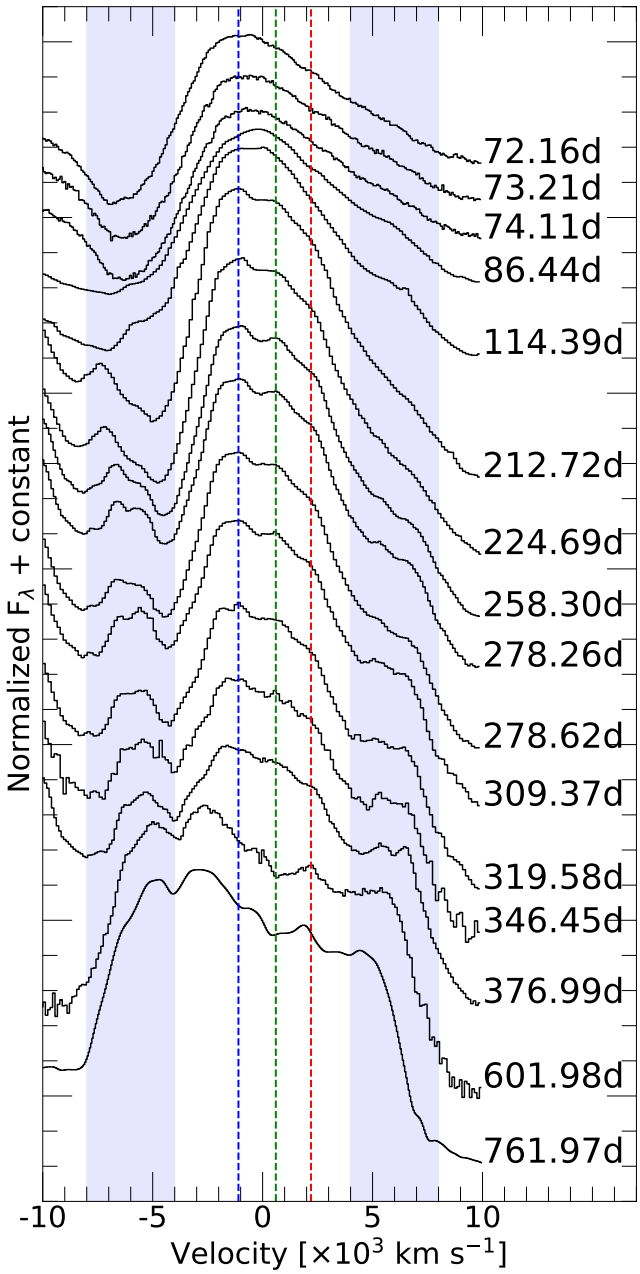

Figure 6. Evolution of the Hα profile from a blueshifted P-Cygni like feature at +72 d to an asymmetric multi–peak feature at +761.97 d, with high velocity components that emerge around +258.30 d. Earlier spectra are presented in (Paper I). All spectra have been corrected for redshift, extinction, and have been continuum subtracted. The blue, green and red vertical lines denote the three shifted peaks located at $\sim -1,100$ km s^{-1}, ~ 600 km s^{-1}, and $\sim 2,200$ km s^{-1} respectively. The blue shaded regions highlight the emerging high-velocity hydrogen features.

and are denoted by the blue, green and red dashed lines in Fig. 6. They show no noticeable velocity evolution between their emergence and the *JWST* epoch at +252.67 d.

A similar Hα evolution has been observed in the nebular phase spectra several other SNe II (e.g. Bevan & Barlow 2016a; Niculescu-Duvaz et al. 2022), including SNe 1987A (Catchpole et al. 1987; Hanuschik 1988; Lucy et al. 1989a), 1999em (Leonard et al. 2002), and 2017gmr (Andrews et al. 2019). As well as the mechanism discussed in Section 7.1, multiple other origins have been proposed to explain multi-peaked Hα features.

Blanketing from an Fe II line has been suggested to cause the asymmetric shape of the Hα (Hoeflich 1988), with addition line blanketing from the Brδ and Brε lines being invoked to explain the shape of the Paα line profile. However, this line blanketing can not be invoked to explain the shape of all the H profiles in SN 2023ixf as several emission lines are isolated from any lines strong enough to cause blanketing, e.g. Brβ and Brγ.

Ejecta asymmetry and the mixing out of ^{56}Ni has also been invoked to explain sloped Hα emission features (Elmhamdi et al. 2003). However, significant amounts of ^{56}Ni mixed within the ejecta would result in ionized CO^+ which appears as an emission peak at 2.26 μm (Spyromilio et al. 1988; Sharp & Hoeflich 1990; Rho et al. 2021), which is not observed in SN 2023ixf.

Between +114.39 and +212.72 d, the Hα in SN 2023ixf develops clear high-velocity blueshifted component, with a weaker high-velocity redshifted component emerging by +258.30 d. These features, which are the same as those mentioned in Section 7.1, are highlighted by the shaded blue regions in Fig. 6. They are roughly symmetrical around the rest wavelength of Hα, with initial velocities of $\sim 8,000 \pm 500$ km s^{-1} when they first emerge. There after, their velocity declines to $\sim 5,000 \pm 500$ km s^{-1} by +761.97 d. This is similar to the late time high-velocity Hα profiles seen in SN 1993J (Matheson et al. 2000), and as discussed in the previous section they may be produced by interaction between a fast moving shock front and low density CSM.

Finally, starting at +212.72 d, as Hα evolves, the red side of the profile becomes attenuated, creating an asymmetrical, sloped emission peak (see Fig. 6). The suppression of the redshifted flux could result from blocking by emission from the receding material. This attenuation may be due to dust formation within the ejecta, as previously suggested for SN 2023ixf (Singh et al. 2024).

7.2.2. *Panchromatic H α-series*

While the study of Hα is useful for understanding the evolution of the H envelope, panchromatic coverage of the H α–series transitions enables a joint time- and wavelength-dependent analysis of the splitting and attenuation across multiple features.

The attenuation of the Hα feature shown in Fig. 6 is also observed in other H emission features, see Fig. 5. The majority of these features exhibit strong attenuation of the redside flux relative to the blueside, most prominently in the α-transitions. The normalized, continuum-subtracted emission features of the Hα, Paα, and Brα transitions for each *JWST* epoch are shown in Fig. 7. For each emission feature, a flat continuum was fit across the bottom to remove the contribution from the IR excess, which significantly affects the shape of the redder emission lines.

All of the features exhibit similar structures, consisting of multiple peaks as highlighted in the previous sections. Additionally, the shapes of the profiles at each epoch are remarkably consistent, with attenuation of the red side of the features that increases over time. This wavelength-dependent analysis allows us to test for dust attenuation, which would one might think would typically affect the bluer emission features over the redder ones. In SN 2023ixf, we observe the same level of attenuation at a given epoch for all the features shown in Fig. 7, regardless of wavelength. The absence of wavelength-dependent attenuation suggests that the shape of these features is not solely due to dust attenuation. However, as we discuss further in Section 8.3, this is in fact is heavily influenced by grain size and dust composition.

7.3. *Oxygen and Calcium Velocity Evolution*

The optical lines of O show a systematic blueshift of $\sim -1,300 \pm 500$ km s^{-1} from the point they first appear in the spectra of SN 2023ixf (see Fig. 8). The blueshift in the optical O profiles is consistent with the shift observed in the H lines. However, the NIR O I 1.1290 μm feature does not show a similar blueshift, which may indicate that these lines form in different regions of the ejecta.

The optical [Ca II] 0.7292, 0.7324 μm doublet and the Ca II NIR triplet exhibit no significant shifts from their rest wavelengths at any epoch shown in Fig. 8, or in other published observations (Singh et al. 2024; Li et al. 2025). However, the Ca features also develops a red side attenuation similar to the hydrogen emission features. This was also observed by (Singh et al. 2024).

7.4. *Neon and Argon Velocity Evolution*

The MIR contains lines from elements that lack emission features at shorter wavelength regions (e.g., Ar and Ne). The *JWST* spectra of SN 2023ixf show two strong lines associated with Ar and Ne, located at 6.985 μm

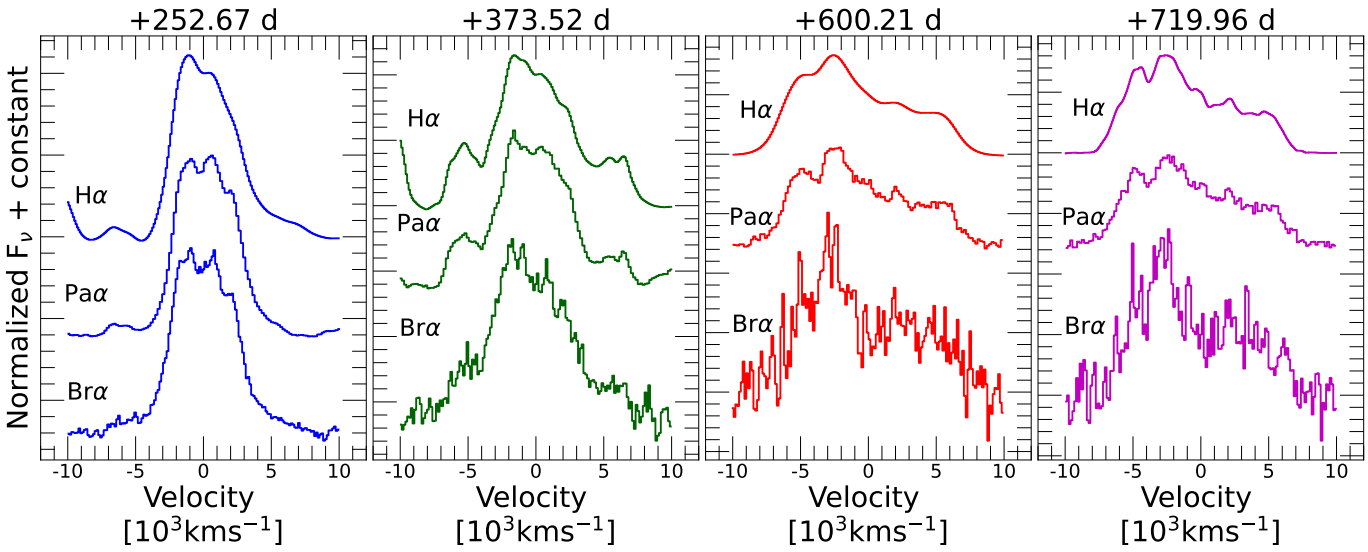

Figure 7. The evolution of the Hα, Paα, and Brα emission features. All features have been continuum-subtracted and normalized to the flux at 0 km s^{-1}. No wavelength-dependent attenuation of the redshifted flux is observed at a given epoch, although a temporal-dependent attenuation is visible.

and 12.813 μm, respectively. The velocity evolution of these lines are presented in Fig. 9.

The [Ar II] 6.985 μm features maintain roughly the same shape and are centered around $0.0 \pm 0.5 \times 10^3$ km s^{-1} in all epochs except at +713.73 d, where the [Ar II] 6.985 μm line shows a slight redshift of $\sim 2,000$ km s^{-1} in its central peak, see in the bottom panel left panel of Fig. 9.

In the first two epochs, the [Ne II] 12.813 μm displays a slightly asymmetric emission feature with an enhanced flux shoulder at $\sim 1,900 \pm 500$ km s^{-1}. This could can be explained by the blending of the [Ne II] line with a weaker emission feature, which is supported by the shape of the [Ne II] 12.813 μm at +600.21 and +713.13 d, where a second peak emerges coincident with the location of the red shoulder, see Fig. 9.

7.5. *Nickel and Cobalt Velocity Evolution*

Deeper within the ejecta, Ni and Co form during the explosive nuclear burning of core-collapse. The [Co II] 10.521 μm line, shown in Fig. 9, exhibits nearly perfect symmetry around 0 km s^{-1} throughout SN 2023ixf's evolution, suggesting that cobalt is centrally located within the ejecta with minimal mixing into the outer regions.

In contrast, the velocity evolution of the [Ni II] 6.636 μm line, also shown in Fig. 9, reveals a tentative blueshift in its emission peak of $\sim 1,000 \pm 500$ km s^{-1}, evolving to $\sim 2,000 - 3,000$ km s^{-1} at +719.96 d. The initial blueshift of the [Ni II] 6.636 μm line mirrors peak velocity seen in the blue peak of the H lines in Fig. 5 and the [O I] 0.6300, 0.6363 μm lines.

7.6. *Nature of the Asymmetrical Ejecta*

Several emission lines in SN 2023ixf, including those from H, O, and Ni, exhibit blue-shifted peaks. While some of this shift could be due to dust obscuring emission from the receding side of the ejecta (see Section 8), the observed asymmetries also point to an intrinsically aspherical explosion geometry (Singh et al. 2024). Aspherical ejecta are common for SNe II and can naturally arise from jet-driven explosion mechanisms (e.g., Khokhlov & Höflich 2001; Scheck et al. 2006; Modjaz et al. 2008; Taubenberger et al. 2009; Milisavljevic et al. 2010; Andrews et al. 2011a; Janka et al. 2016; Tucker et al. 2024). In such scenarios, a significant fraction of the ejecta moves toward the observer, resulting in a net blue shift. The observed flux asymmetry around the rest wavelengths of the lines provides a direct probe of the degree of asymmetry in the explosion.

In SN 2023ixf the shifts in emission peaks we observe could also result from an asymmetric distribution of ^{56}Ni within the ejecta (Gerardy et al. 2000; Utrobin & Chugai 2017; Bose et al. 2019). In this scenario, uneven heating of the surrounding O-rich material by ^{56}Ni would lead to asymmetric oxygen emission features (Gerardy et al. 2000; Maeda et al. 2008). However, we disfavor this interpretation due to the symmetric profile of the [Co II] 10.521 μm line and the absence of CO^+, which forms through mixing between the CO and ^{56}Ni-rich regions.

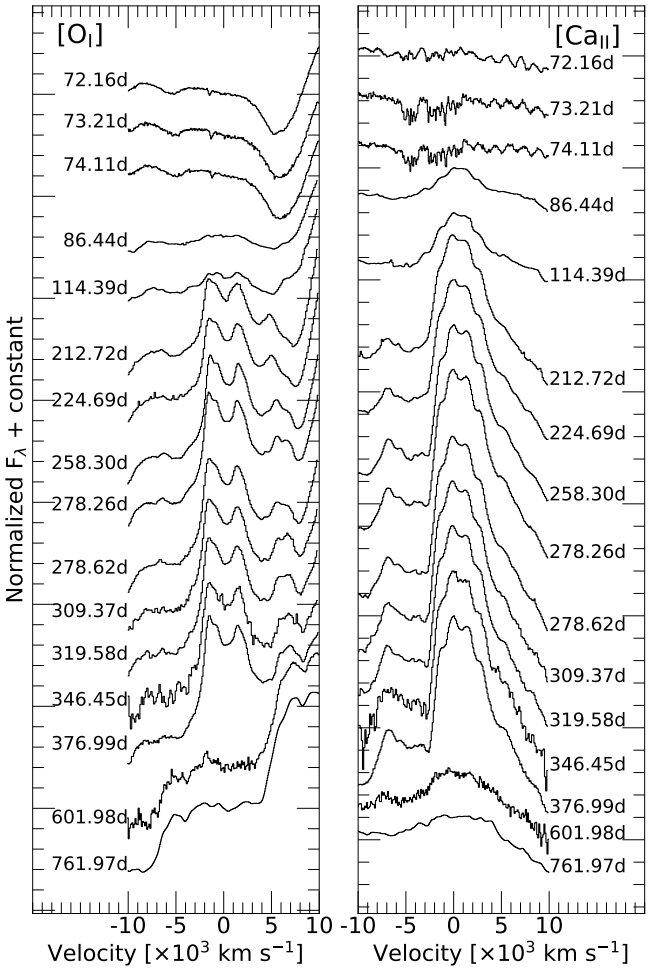

Figure 8. Spectral evolution of the [O I] 0.6300, 0.6363 μm doublet and [Ca II] 0.7292 0.7324 μm. The features are plotted in velocity space relative to the rest-frame wavelengths of the [O I] 0.6300 μm and [Ca II] 0.7292 μm lines, respectively. The [O I] 0.6300, 0.6363 μm features show a significant blueshift of $\sim 1,300 \pm 500$ km s^{-1}, similar to the blue peak observed in the split H emission peak, while the [Ca II] 0.7292 0.7324 μm remains centered at the rest wavelength. The difference in the location of the peaks suggests that the O and Ca are located in drastically different regions of the SN ejecta.

The discrepancy between the blueshifted O lines and the symmetrical line profiles observed in other species, such as Ca, and Co, could also be explained as a combination of a high-density clump, or torus, of O-rich material interacting with the equatorial dense CSM moving along our line of sight and a bulk ejecta distributed around 0 km s^{-1} (Fang et al. 2024; Ferrari et al. 2024; Kumar et al. 2025). This ejecta structure was first observed in SN 1987A (Li & McCray 1992) and has since been identified in several other SNe (Milisavljevic et al. 2010; Kuncarayakti et al. 2020; Fang et al. 2022).

Although an aspherical explosion geometry explains the systematic blueshifts observed in the O and Ni emission profiles, it does not account for the evolving morphology of the H-series lines, which have a time dependent attenuation of the red-side flux and multiple peaks. This requires interaction with a clumpy CSM and possibly dust formation in the ejecta.

8. ORIGIN OF THE DUST EMISSION

While it is clear that dust plays a significant role in the evolution of SN 2023ixf, determining the origin of this dust is not straightforward. As noted in Section 4, the +252.67 d spectrum of SN 2023ixf shows a strong, featureless IR excess. By +373.52 d, a broad continuum feature develops around 10.0 μm, which remains present in subsequent epochs. The IR continuum of SN 2023ixf does not change again significantly until +719.96 d, when a second peak emerges at $\sim$18.0 μm. These peaks, at $\sim$10.0 μm and $\sim$18.0 μm, are indicative of silicate-rich dust (Shahbandeh et al. 2023).

The evolving SED of SN 2023ixf can be explained by several possible sources of dust (see Fig. 5 in Sarangi et al. 2018), including: 1) pre-existing dust in the CSM located beyond the explosion's evaporation radius (Bode & Evans 1980; Dwek 1983; Andrews et al. 2011b); 2) freshly formed dust in the cool dense shell (CDS) between the forward and reverse shocks (Pozzo et al. 2004; Smith et al. 2008; Gall et al. 2014); and 3) newly condensed dust within the SN ejecta itself (Kotak et al. 2005; Andrews et al. 2011a; Szalai & Vinkó 2013). Although determining the precise dust properties of SN 2023ixf requires detailed modeling, which we reserved for a future paper in this series, we discuss the plausibility of each dust source below.

8.1. *Pre-existing CSM Dust*

The first option is that the IR excess originates from pre-existing dust located outside the evaporation radius of the explosion. This dust is heated by the shock breakout emission and, as the dust evolves, transitions from optically thick to optically thin causing the shape of the IR emission to change (Sarangi et al. 2018; Shahbandeh et al. 2023). This dust would reside in the CSM of the progenitor, or the interaction region between CSM and the ISM (Dragulin & Hoeflich 2016).

At +252.67 d, the infared continuum is well approximated by a black body of a temperature of 688 K, which is well below the evaporation temperature for both carbonates and silicates, hence it is produced from warm dust. Assuming an optically thick and spherical dust distribution, a dust temperature of 688 K would correspond to a radius of $r_{dust} = 2.2 \times 10^{16}$ cm. A similar value, $r_{dust} \sim 1.6 \times 10^{16}$ cm, was suggested from

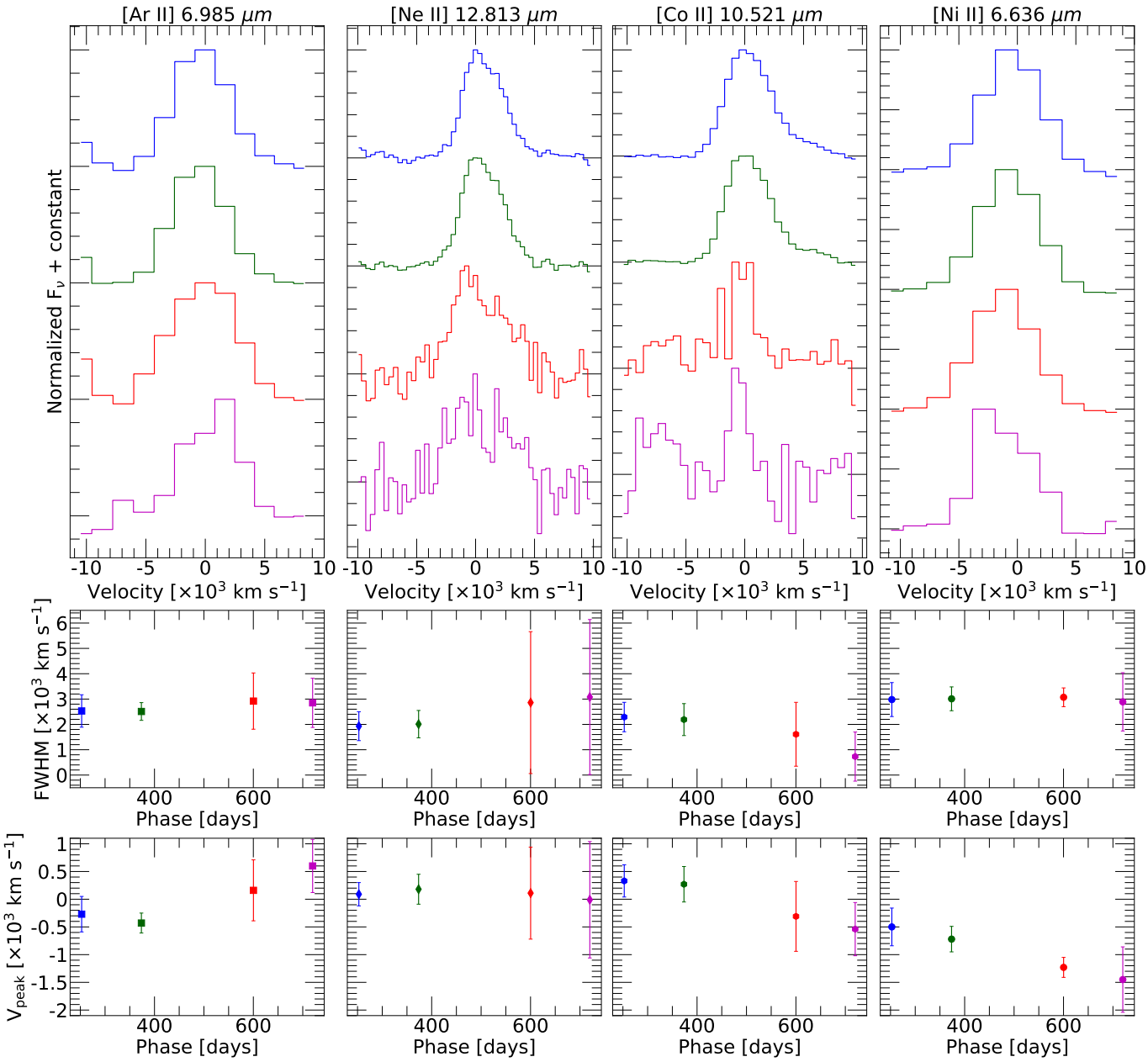

Figure 9. Velocity evolution of the [Ni II] 6.636 μm, [Ar II] 6.985 μm, [Co II] 10.521 μm, and [Ne II] 12.813 μm. While the neon, argon, and cobalt lines are centered around 0 km s^{-1}, the nickel emission feature is blueshifted by $\sim 1,000 \pm 500$ km s^{-1} at all epochs. All emission features have been corrected by removing a linear continuum across the bottom of the features to remove the influence of the IR excess, especially at late times when the lines are weaker. The FWHM and peak velocity determined by Gaussian fits are shown in the middle and bottom row, respectively

a 700 K blackbody fit to the 3.4 μm NEOWISE photometry at +212 d (Van Dyk et al. 2024a). For SNe II, the typical photospheric radius is $1 - 10 \times 10^{14}$ cm (e.g. Hoeflich 1988; Dessart & Hillier 2005), with photospheric temperatures of $5,000 - 10,000$ K. New dust forms once the ejecta drops below the evaporation temperature, and would reside close to the photosphere, assuming $T_{dust} \propto \sqrt{R_{ph}}$, while heated dust should be located further out, $\approx 100\ R_{ph}$.

Moreover, the CSM distance derived from the X-ray emission, $< 7 \times 10^{15}$ cm is likely produced in the low density region ($100 - 10,000$ times the ISM density) and by the interaction between the reverse shock and the wind-like CSM (Margutti et al. 2012; Dragulin & Hoeflich 2016; Grefenstette et al. 2023; Panjkov et al. 2024; Nayana et al. 2025). High-velocity ejecta from the SNe ($\gtrsim 30,000$ km s^{-1}) would traverse the CSM with minimal deceleration, reaching radii of $\sim 2 \times 10^{16}$ cm

within a few months. This rapid interaction would be expected to cause dust evaporation, producing an infrared component near the dust sublimation temperature ($T \gtrsim 2000$ K), in contrast to the warm dust (688 K) temperatures that are actually observed. Given this, the ejecta is unlikely to have reached the dust region, even by +250 d, placing the dust at distances similar to the estimate from the infrared continuum. In reality, the CSM is likely not a spherical shell and is likely clumpy, meaning that 2.2×10^{16} cm should only be taken as a strict lower limit. An asymmetric clumpy CSM is also supported by the X-ray and radio observations, which require significant clumping to find agreement in the derived X-ray and radio CSM density profiles (Panjkov et al. 2024; Nayana et al. 2025). Future, detailed analysis is required to determine the exact location and nature of the dust.

8.2. *Cold Dense Shell Dust*

The second mechanism involves the formation of dust within the CDS produced in the post-shocked CSM. As the forward shock moves through the surrounding CSM and the reverse shock traverses into the inner ejecta, material is built up, shocked and heated. This postshock gas then rapidly cools, through a combination of free-free and molecular/atomic line cooling, forming a CDS sufficiently cool and dense enough to facilitate the formation of dust (Sarangi et al. 2018). This dust is heated by ionizing photons from the forward shock, with dust above 2000 K rapidly subliming after formation. It may be assumed that, given the temperature dependence, the CDS is unlikely to be the cause of the initial IR excess observed at $t < 250$ d as the heating from the forward shock would inhibit dust formation (Sarangi et al. 2018). At later times, as the shock luminosity declines, the gas temperature in the CDS becomes conducive to dust formation. However, for CDS dust to account for the observed attenuated line profiles (if they are not produced from a geometry effect) it would need to be mixed into the ejecta.

8.3. *Ejecta Dust*

The third location for dust formation is within the expanding SN ejecta interior to the reverse shock. Dust can be formed within the ejecta once the temperature drops below the condensation temperature. This is facilitated by emission from molecular ro-vibrational bands, features that are observed in the spectra as early as +252.67 d. While ejecta dust could explain the late-time IR excess, the ejecta temperature would be too high at earlier phases to allow for dust formation (Singh et al. 2024). For example, in some instances, in situ dust formation is not expected to occur until at least 450 d after the explosion (Sarangi 2022).

One hallmark of dust formation in the ejecta is the attenuation of the red side of optical emission features (Gall et al. 2014). This is clearly observed in the Hα series and [Ca II] 0.7292 0.7324 μm, line profiles. For SN 2023ixf, we also observe time-dependent attenuated profiles in the Pashen-α and Brackett-α features, suggesting that this is not a wavelength-dependent effect (at least between 0.5–4 μm). While one might expect dust blocking to show a strong wavelength dependence, given the blue Rayleigh scattering, previous studies have examined this issue. Lucy et al. (1989b) considered the effects of scattering via dust albedo and concluded that, for SN 1987A, scattering was negligible. They also inferred a grain size of $a \leq 0.05$ μm. In the DAMOCLES code (Bevan & Barlow 2016b; Bevan 2018), scattering is modeled using the Henyey-Greenstein phase function, and no significant variations are observed across the Balmer lines (Bevan & Barlow 2016b, see their Figure 9). While we acknowledge the possibility of dust producing a wavelength-dependent blocking effect, the literature does not find a strong wavelength dependence for the lines we observe in SN 2023ixf, and we defer further conclusions to future work in the series.

8.4. *The Full Picture*

In reality, a combination of dust formation processes may be required to explain the observed properties of SN 2023ixf. The strong IR excess at +252.67 suggests the presence of dust either in the CSM or CDS. Given the dusty nature of the progenitor, significant heating of pre-existing dust in the CSM might be expected.

The evolution of the line profiles may also indicate that some dust may be present within the ejecta. This dust may form as the ejecta cools below the condensation temperature or originate in the CDS and subsequently mix into the ejecta (Bevan et al. 2019; Singh et al. 2024). The latter scenario implies a clumpy dust structure. However, these profiles could also be produced by geometry effects and detailed modeling is needed to distinguish between these possibilities.

Overall, we tentatively suggest that the IR excess in SN 2023ixf results from a combination of pre-existing dust in the CDS or pre-existing in the CSM, which dominates at early times, and newly formed dust, which becomes more prominent at later epochs. This newly formed dust likely originates from either within the ejecta, in a clumpy CDS that mixes into the ejecta, or a combination of both. We will examine this is more detail in the next papers of the series.

9. CONCLUSIONS

Here we present the panchromatic dataset of SN 2023ixf spanning from $0.32 - 30.0$ μm between $+252.67 - +719.96$ d past explosion, with optical data spanning from +72.16 to +224.69 d. This is the most complete *JWST* time series of a SN II to date. In this second paper of our series, we concentrate on presenting this exquisite dataset, as well as identifying the predominant spectral lines and molecular bands that form in the ejecta. The data presented here were obtained from the NIRSpec, and MIRI-LRS, and MIRI-imager instruments, and supplemented with data from a variety of ground based telescopes, allowing us to construct $0.32 - 30$ μm panchromatic SED's. The main results from our work are as follows:

- The *JWST* spectra of SN 2023ixf reveal a rich array of atomic species, including rare members of the hydrogen Brackett, Pfund, and Humphreys series, as well as forbidden lines from Co, Ni, Fe, Ne, and Ar. C, O, Mg, Na, and Ca lines are also present in SN 2023ixf at shorter wavelengths (see § 5).

- SN 2023ixf shows significant features of CO formation, visible by the first overtone and fundamental ro-vibrational bands, which were not present in the earlier *JWST* spectrum (Paper I). While the first overtone fades by +600.21 d, the fundamental band remains detectable at all epochs, indicating the CO region is dropping in temperature below 1000 K (see § 5.12).

- The splitting of late-time H lines from the Balmer, Pashen, and Brackett series into multiple features suggests that SN 2023ixf was likely a highly asymmetric explosion with a disk-like CSM. Additional high-velocity features, linked to an aspherical shock front, are also observed (see § 7.2).

- Several emission lines in SN 2023ixf (e.g., from H, O, and Ni) exhibit blueshifted peaks, consistent with an aspherical, clumpy explosion geometry. A high density clumpy or toroidal distribution of O-rich material expanding along the line of sight, combined with Ca- and ^{56}Ni-rich regions aligned perpendicular to the observer, explains the observed blueshifts and the lack of velocity shifts in Ca and Co lines (see § 7.6).

- The SED of SN 2023ixf shows a time evolving IR dust component which emerges by +252.67 d, with distinct features indicative of Si-rich dust appearing at 10 μm by +373.52 d and 18 μm by +719.96 d (see § 4).

- The initial (+252.67 d) featureless IR continuum may be explained by the presence of pre-existing dust located outside the evaporation radius of the SN 2023ixf, which is consistent with the dusty nature of the RSG progenitor star (see § 8).

- The time-evolving obscuration of the red side of Hα, Pashen-α, Brackett-α, and [Ca II] 0.7292 0.7324 μm may be explained by the start of dust formation, or as a result of an aspherical explosion geometry. If the attenuation is caused by dust, it may have formed within the ejecta or in a clumpy, cold, dense shell that mixes into the ejecta (see § 8).

- We tentatively suggest the IR excess observed in SN 2023ixf arises from a combination of pre-existing, likely Si-rich, dust in the CSM or CDS, dominant at early times, and newly formed either dust within the ejecta or in a clumpy CDS that mixes into the ejecta (see § 8). Although, detailed models are required to explore this further.

While it is beyond the scope of this paper to determine the exact grain size, mass, and location of the dust, such early emission of dust suggests that some amount of pre-existing dust ejected by the RSG progenitor can survive within the CSM and survive the forward shock of the explosion. However, disentangling the exact location of the dust (CSM vs CDS vs ejecta), is left for a more detailed analysis, which will be presented in future papers of this series.

Overall, *JWST* has allowed the MIR region of the electromagnetic spectrum to be explored in unprecedented detail. In this paper, the second in the series, we have presented nebular phase panchromatic data of SN 2023ixf and demonstrated how this data can be used to explore the line formation processes in the various wavelength regions in the ejecta. In future papers, we will focus on both molecule and dust modeling of the respective features, determining their properties, mass, and location, and examine how this links to the progenitor system. SN 2023ixf is becoming one of the best observed SNe II to date, and future scheduled *JWST* and ground based observations will ensure this truly amazing dataset continues to improve.

ACKNOWLEDGMENTS

K.M., E.B., C.A., J.D., M.S., P.H., and A.V.F. acknowledge support from NASA grants JWST-GO-02114,

JWST-GO-02122, JWST-GO-04522, JWST-GO-04217, JWST-GO-04436, JWST-GO-03726, JWST-GO-05057, JWST-GO-05290, JWST-GO-06023, JWST-GO-06677, JWST-GO-06213, JWST-GO-06583. Support for programs #2114, #2122, #3726, #4217, #4436, #4522, #5057, #6023, #6213, #6583, and #6677 were provided by NASA through a grant from the Space Telescope Science Institute, which is operated by the Association of Universities for Research in Astronomy, Inc., under NASA contract NAS 5-03127.

Some of this material is based upon work supported by the National Science Foundation Graduate Research Fellowship Program under Grant Nos. 1842402 and 2236415, and NSF award AST-230639 to P.H.. Any opinions, findings, conclusions, or recommendations expressed in this material are those of the author(s) and do not necessarily reflect the views of the National Science Foundation.

D.O.J. acknowledges support from NSF grants AST-2407632 and AST-2429450, NASA grant 80NSSC24M0023, and HST/JWST grants HST-GO-17128.028, HST-GO-16269.012, and JWST-GO-05324.031, awarded by the Space Telescope Science Institute (STScI), which is operated by the Association of Universities for Research in Astronomy, Inc., for NASA, under contract NAS5-26555.

M.D. Stritzinger is funded by the Independent Research Fund Denmark (IRFD, grant number 10.46540/2032-00022B) and by an Aarhus University Research Foundation Nova project (AUFF-E-2023-9-28).

A.V.F. is grateful to the Christopher R. Redlich Fund for additional support.

L.G. acknowledges financial support from AGAUR, CSIC, MCIN and AEI 10.13039/501100011033 under projects PID2023-151307NB-I00, PIE 20215AT016, CEX2020-001058-M, ILINK23001, COOPB2304, and 2021-SGR-01270.

Based on observations made with the Gran Telescopio Canarias (GTC), installed at the Spanish Observatorio del Roque de los Muchachos of the Instituto de Astrofísica de Canarias, on the island of La Palma.

The Shappee group at the University of Hawai'i is supported with funds from NSF (grants AST-2407205) and NASA (grants HST-GO-17087, 80NSSC24K0521, 80NSSC24K0490, 80NSSC23K1431).

JTH was supported by NASA grant 80NSSC23K1431.

Parts of this research were supported by the Australian Research Council Centre of Excellence for Gravitational Wave Discovery (OzGrav), through project number CE230100016.

SZ received support from the NKFIH OTKA K142534 grant.

Parts of this research were supported by the Australian Research Council Centre of Excellence for Gravitational Wave Discovery (OzGrav), through project number CE230100016.

D.M. acknowledges support from the National Science Foundation (NSF) through grants PHY-2209451 and AST-2206532.

Facilities: JWST(NIRSpec and MIRI), INT(IDS), IRFT(Spex), GTC(OSIRIS+ and EMIR), Keck:I(LRIS), Keck:II(NIRES), UH:2.2m(SNIFS)

Software: `Astropy` (Astropy Collaboration et al. 2013), `Dust-extinction` (Gordon et al. 2023; Gordon 2023), *JWST* reduction notebooks (Law et al. 2025), *JWST* Science Calibration Pipeline (ver. 1.18.0; (Bushouse et al. 2022)), `Matplotlib` (Hunter 2007), `Numpy` (Harris et al. 2020), `SciPy` (Virtanen et al. 2020), `Sextractor` (Burrow et al. 2020)

APPENDIX

A. OBSERVATION LOG AND GB-SPECTRA

Here we provide detailed logs of all of the observations, analysis, and results used in this work. The JWST, groundbase optical and NIR spectral observations are presented in Tables A1, and A2 respectively.

In addition, we show the full wavelength coverage of the ground based optical and NIR spectra of SN 2023ixf obtained between $+72.16 - 761.97$ d. These spectra are shown in Figs. A1 and A2, respectively.

REFERENCES

Abac, A. G., Abbott, R., Abouelfettouh, I., et al. 2025, ApJ, 985, 183, doi: 10.3847/1538-4357/adc681

Aldering, G., Adam, G., Antilogus, P., et al. 2002, in Society of Photo-Optical Instrumentation Engineers (SPIE) Conference Series, Vol. 4836, Survey and Other Telescope Technologies and Discoveries, ed. J. A. Tyson & S. Wolff, 61–72, doi: 10.1117/12.458107

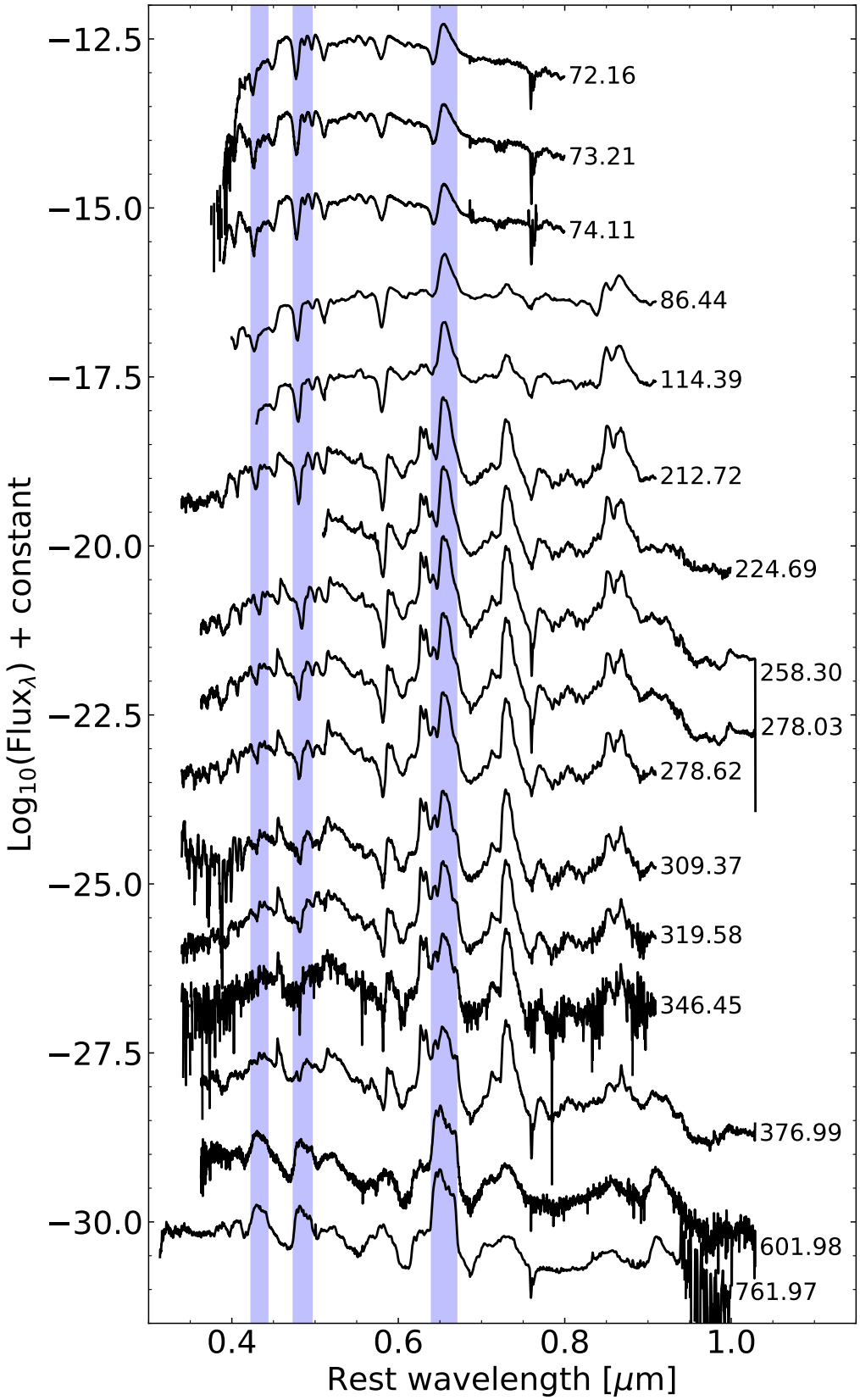

Figure A1. The optical spectral time series of SN 2023ixf used in this work. All spectra have been corrected for redshift and extinction. The phase relative to the explosion date is given for each spectrum on the right. The emission regions of the Hα, Hβ, and Hγ lines are highlighted by the blue regions.

Table A1. Log of *JWST* spectroscopic observations

Parameter	Visit 2	Visit 3	Visit 4	Visit 5
NIRSpec Spectral Observations				
Mode	Fixed Slit	Fixed Slit	Fixed Slit	Fixed Slit
Slit	S400A1	S400A1	S400A1	S400A1
Grating / Filter	G235M-F170LP/ G395M-F290LP	G235M-F170LP/ G395M-F290LP	G235M-F170LP/ G395M-F290LP	G235M-F170LP/ G395M-F290LP
Exp Time / dither (s)	63.90/63.90	157.38/157.38	163.61/126.22	163.61/126.22
Phase (days)	252.66/252.65	373.52/373.51	600.21/600.20	722.90/722.98
$T_{\rm obs}$ (MJD)	60335.61/60335.60	60456.57/60456.56	60683.44/60683.42	60806.23/60806.22
MIRI Spectral Observations				
Mode	LRS	LRS	LRS	LRS
Exp Time / Dither (s)	255.30	505.06	277.50	277.50
Phase (days)	252.69	373.54	600.23	714.08
$T_{\rm obs}$ (MJD)	60335.64	60456.58	60683.46	714.08

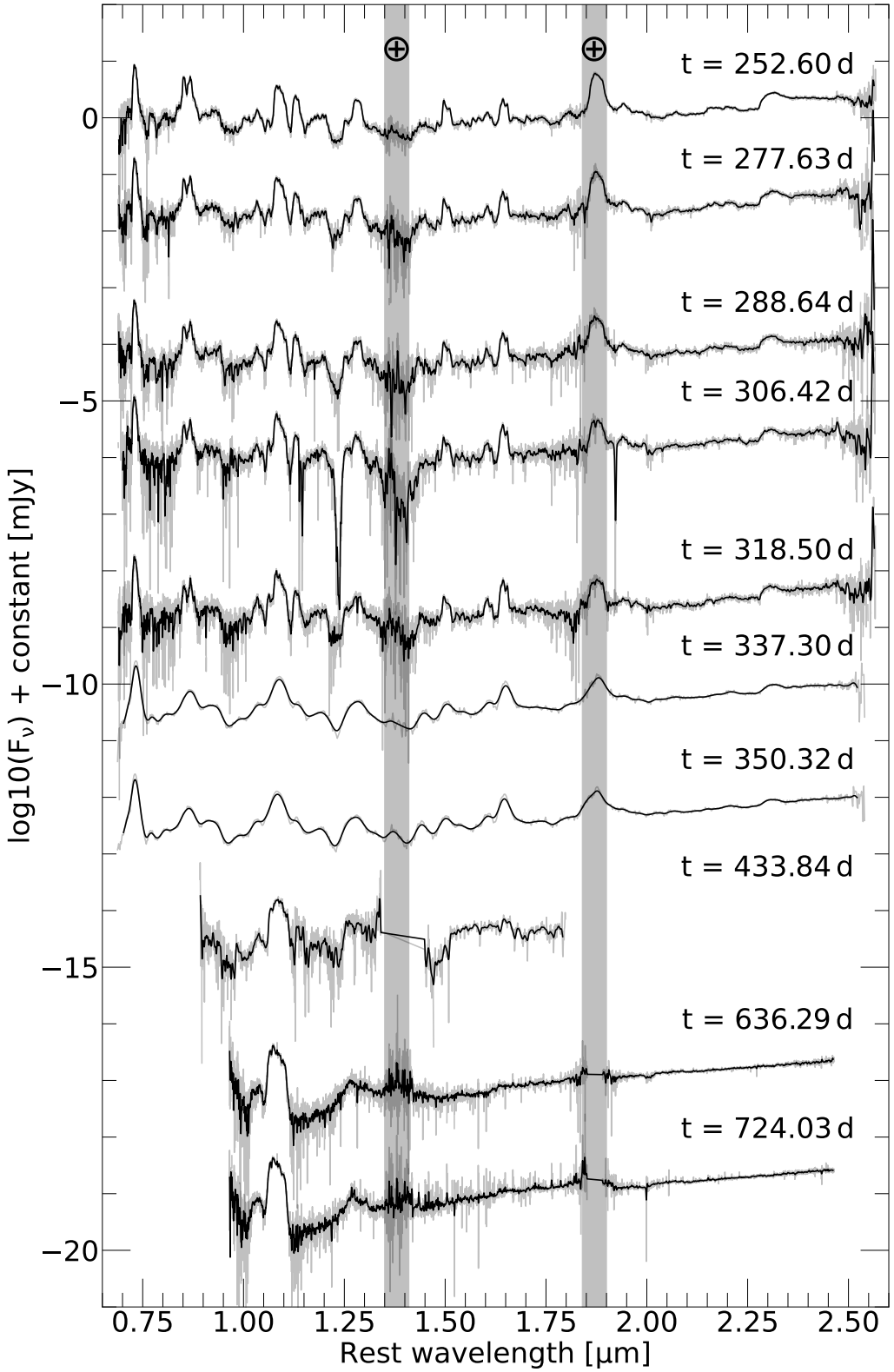

Figure A2. IRTF/SpeX and Keck/NIRES spectra of SN 2023ixf between 250 and 725 d. The telluric regions are highlighted by the gray regions. As SN 2023ixf evolved, the CO first overtone feature, $2.2 - 2.5$ μm, declined in strength, and a strong IR excess developed in the NIR continuum above ~ 1.2 μm, corresponding to hot dust.

Table A2. Log of GB-optical and NIR spectra of SN 2023ixf obtained between $+250 - +765$ d. All phases are given in rest frame

Obs. Date [MJD]	Phase [$days$]	Exp. Time [s]	Telescope/Instrument
		Optical-spectra	
60154.97	72.16	600	INT/IDS
60155.02	73.21	600	INT/IDS
60156.92	74.11	2 × 600	INT/IDS
60169.26	86.44	2 × 1800	UH88/SNIFS
60197.23	114.39	1800	UH88/SNIFS
60295.64	212.72	1800	UH88/SNIFS
60307.62	224.69	1800	UH88/SNIFS
60340	258.39	2 × 900	GTC/OSIRIS+
60361	278.03	4 × 450	GTC/OSIRIS+
60361.59	278.62	2× 1800	UH88/SNIFS
60392.37	309.37	1800/1200	UH88/SNIFS
60402.59	319.58	1800	UH88/SNIFS
60429.48	346.45	1800	UH88/SNIFS
60459	375.95	2 × 600	GTC/OSIRIS+
60685	601.77	4 × 500	GTC/OSIRIS+
60845.33	761.97	6 × 1800 / 12 × 900	Keck-I/LRIS
		NIR-spectra	
60335.55	252.60	44 × 120	IRTF/SpeX
60360.60	277.63	14 × 120	IRTF/SpeX
60371.62	288.64	8 × 120	IRTF/SpeX
60389.42	306.42	18 × 120	IRTF/SpeX
60401.50	318.50	30 × 120	IRTF/SpeX
60420.32	337.30	14 × 120[a]	IRTF/SpeX
60433.35	350.32	10 × 120[a]	IRTF/SpeX
60516.94	433.84	121	GTC/EMIR
60719.55	636.29	12 × 300.0	Keck-II/NIRES
60807.36	724.03	22 × 300.0	Keck-II/NIRES

NOTE—[a] - Denotes observations taken in PRISM mode of IRTF/SpeX

Alvarez, P., Rodríguez Espinosa, J. M., & Sánchez, F. 1998, NewAR, 42, 553, doi: 10.1016/S1387-6473(98)00071-2
Anderson, J. P., Dessart, L., Gutierrez, C. P., et al. 2014, MNRAS, 441, 671, doi: 10.1093/mnras/stu610
Andrews, J. E., Sugerman, B. E. K., Clayton, G. C., et al. 2011a, ApJ, 731, 47, doi: 10.1088/0004-637X/731/1/47
Andrews, J. E., Clayton, G. C., Wesson, R., et al. 2011b, AJ, 142, 45, doi: 10.1088/0004-6256/142/2/45
Andrews, J. E., Sand, D. J., Valenti, S., et al. 2019, ApJ, 885, 43, doi: 10.3847/1538-4357/ab43e3
Arnett, W. D., Bahcall, J. N., Kirshner, R. P., & Woosley, S. E. 1989, ARA&A, 27, 629, doi: 10.1146/annurev.aa.27.090189.003213
Ashall, C., Baron, E., DerKacy, J. M., et al. 2023a, Dust Our Luck? Measuring Molecule and Dust Formation in M101's Hydrogen-rich SN 2023ixf, JWST Proposal. Cycle 2, ID. #4575
—. 2023b, Dust Our Luck? Measuring Molecule and Dust Formation in M101's Hydrogen-rich SN 2023ixf, JWST Proposal. Cycle 1, ID. #4522
Ashall, C., Hoeflich, P., Baron, E., et al. 2024a, ApJ, 975, 203, doi: 10.3847/1538-4357/ad6608
Ashall, C., Hoeflich, P. A., Shahbandeh, M., et al. 2024b, Building the Legacy of Supernova 2023ixf: How Does Molecule Formation Lead to Dust?, JWST Proposal. Cycle 3, ID. #5290
Astropy Collaboration, Robitaille, T. P., Tollerud, E. J., et al. 2013, A&A, 558, A33, doi: 10.1051/0004-6361/201322068
Baron, E., et al. 2025, ApJ, submitted
Berger, E., Keating, G. K., Margutti, R., et al. 2023, ApJL, 951, L31, doi: 10.3847/2041-8213/ace0c4
Bersten, M. C., Orellana, M., Folatelli, G., et al. 2024, A&A, 681, L18, doi: 10.1051/0004-6361/202348183
Bevan, A. 2018, MNRAS, 480, 4659, doi: 10.1093/mnras/sty2094
Bevan, A., & Barlow, M. J. 2016a, MNRAS, 456, 1269, doi: 10.1093/mnras/stv2651
—. 2016b, MNRAS, 456, 1269, doi: 10.1093/mnras/stv2651
Bevan, A., Wesson, R., Barlow, M. J., et al. 2019, MNRAS, 485, 5192, doi: 10.1093/mnras/stz679
Biscaro, C., & Cherchneff, I. 2014, A&A, 564, A25, doi: 10.1051/0004-6361/201322932
Bode, M. F., & Evans, A. 1980, MNRAS, 193, 21P, doi: 10.1093/mnras/193.1.21P
Böker, T., Beck, T. L., Birkmann, S. M., et al. 2023, PASP, 135, 038001, doi: 10.1088/1538-3873/acb846
Bose, S., Dong, S., Elias-Rosa, N., et al. 2019, ApJL, 873, L3, doi: 10.3847/2041-8213/ab0558
Bostroem, K. A., Pearson, J., Shrestha, M., et al. 2023, ApJL, 956, L5, doi: 10.3847/2041-8213/acf9a4
Burrow, A., Baron, E., Ashall, C., et al. 2020, ApJ, 901, 154, doi: 10.3847/1538-4357/abafa2
Bushouse, H., Eisenhamer, J., Dencheva, N., et al. 2022, JWST Calibration Pipeline, Tech. rep., doi: 10.5281/zenodo.7038885
Cardiel, N., Pascual, S., Gallego, J., et al. 2019, in Astronomical Society of the Pacific Conference Series, Vol. 523, Astronomical Data Analysis Software and Systems XXVII, ed. P. J. Teuben, M. W. Pound, B. A. Thomas, & E. M. Warner, 317
Catchpole, R., Glass, I., Karovska, M., et al. 1987, IAUC, 4457, 1
Chandra, P., Chevalier, R. A., Maeda, K., Ray, A. K., & Nayana, A. J. 2024, ApJL, 963, L4, doi: 10.3847/2041-8213/ad275d
Chevalier, R. A., & Fransson, C. 1987, Nature, 328, 44, doi: 10.1038/328044a0
Chiar, J. E., & Tielens, A. G. G. M. 2006, ApJ, 637, 774, doi: 10.1086/498406
Clayton, D. D., Deneault, E. A. N., & Meyer, B. S. 2001, ApJ, 562, 480, doi: 10.1086/323467
Clayton, G. C., Wesson, R., Fox, O. D., et al. 2025, arXiv e-prints, arXiv:2505.01574, doi: 10.48550/arXiv.2505.01574
Cushing, M. C., Vacca, W. D., & Rayner, J. T. 2004, PASP, 116, 362, doi: 10.1086/382907
Davis, S., Hsiao, E. Y., Ashall, C., et al. 2019, ApJ, 887, 4, doi: 10.3847/1538-4357/ab4c40
DerKacy, J., et al. 2025, ApJ, submitted
Dessart, L., & Hillier, D. J. 2005, A&A, 437, 667, doi: 10.1051/0004-6361:20042525
Dragulin, P., & Hoeflich, P. 2016, ApJ, 818, 26, doi: 10.3847/0004-637X/818/1/26
Dwek, E. 1983, ApJ, 274, 175, doi: 10.1086/161435
Dwek, E. 2006, Science, 313, 178, doi: 10.1126/science.1130423
Dwek, E., Galliano, F., & Jones, A. P. 2007, ApJ, 662, 927, doi: 10.1086/518430
Dwek, E., & Scalo, J. M. 1980, ApJ, 239, 193, doi: 10.1086/158100
Dyer, M. J., Ackley, K., Jiménez-Ibarra, F., et al. 2024, in Society of Photo-Optical Instrumentation Engineers (SPIE) Conference Series, Vol. 13094, Ground-based and Airborne Telescopes X, ed. H. K. Marshall, J. Spyromilio, & T. Usuda, 130941X, doi: 10.1117/12.3018305
Elmhamdi, A., Danziger, I. J., Chugai, N., et al. 2003, MNRAS, 338, 939, doi: 10.1046/j.1365-8711.2003.06150.x

Ercolano, B., Barlow, M. J., & Sugerman, B. E. K. 2007, MNRAS, 375, 753, doi: 10.1111/j.1365-2966.2006.11336.x
Fan, X., Strauss, M. A., Schneider, D. P., et al. 2003, AJ, 125, 1649, doi: 10.1086/368246
Fang, Q., Maeda, K., Kuncarayakti, H., & Nagao, T. 2024, Nature Astronomy, 8, 111, doi: 10.1038/s41550-023-02120-8
Fang, Q., Maeda, K., Kuncarayakti, H., et al. 2022, ApJ, 928, 151, doi: 10.3847/1538-4357/ac4f60
Fedriani, R., Caratti o Garatti, A., Koutoulaki, M., et al. 2020, A&A, 633, A128, doi: 10.1051/0004-6361/201936748
Ferrari, L., Folatelli, G., Ertini, K., Kuncarayakti, H., & Andrews, J. E. 2024, A&A, 687, L20, doi: 10.1051/0004-6361/202450440
Ferrarotti, A. S., & Gail, H. P. 2006, A&A, 447, 553, doi: 10.1051/0004-6361:20041198
Flinner, N., Tucker, M. A., Beacom, J. F., & Shappee, B. J. 2023, Research Notes of the American Astronomical Society, 7, 174, doi: 10.3847/2515-5172/acefc4
Folatelli, G., Ferrari, L., Ertini, K., Kuncarayakti, H., & Maeda, K. 2025, A&A, 698, A213, doi: 10.1051/0004-6361/202554128
Fox, O., Szalai, T., Van Dyk, S. D., et al. 2024, Building A Modern Sample of Dusty Supernovae with JWST, JWST Proposal. Cycle 2, ID. #3921
Gall, C., Hjorth, J., & Andersen, A. C. 2011, A&A Rv, 19, 43, doi: 10.1007/s00159-011-0043-7
Gall, C., Hjorth, J., Watson, D., et al. 2014, Nature, 511, 326, doi: 10.1038/nature13558
Garzón, F., Balcells, M., Gallego, J., et al. 2022, A&A, 667, A107, doi: 10.1051/0004-6361/202244729
Gerardy, C. L., Fesen, R. A., Höflich, P., & Wheeler, J. C. 2000, AJ, 119, 2968, doi: 10.1086/301390
Gordon, K. 2023, karllark/dust_extinction: OneRelationForAllWaves, v1.2, Zenodo, Zenodo, doi: 10.5281/zenodo.7799360
Gordon, K. D., Clayton, G. C., Decleir, M., et al. 2023, ApJ, 950, 86, doi: 10.3847/1538-4357/accb59
Grefenstette, B. W., Brightman, M., Earnshaw, H. P., Harrison, F. A., & Margutti, R. 2023, ApJL, 952, L3, doi: 10.3847/2041-8213/acdf4e
Groot, P. J., Bloemen, S., Vreeswijk, P. M., et al. 2022, in Society of Photo-Optical Instrumentation Engineers (SPIE) Conference Series, Vol. 12182, Ground-based and Airborne Telescopes IX, ed. H. K. Marshall, J. Spyromilio, & T. Usuda, 121821V, doi: 10.1117/12.2630160
Guetta, D., Langella, A., Gagliardini, S., & Della Valle, M. 2023, ApJL, 955, L9, doi: 10.3847/2041-8213/acf573
Hanuschik, R. W. 1988, PASA, 7, 446, doi: 10.1017/S1323358000022621
Harris, C. R., Millman, K. J., van der Walt, S. J., et al. 2020, Nature, 585, 357, doi: 10.1038/s41586-020-2649-2
Hiramatsu, D., Tsuna, D., Berger, E., et al. 2023, ApJL, 955, L8, doi: 10.3847/2041-8213/acf299
Hoeflich, P. 1988, PASA, 7, 434, doi: 10.1017/S1323358000022608
Hoogendam, W. B., Jones, D. O., Ashall, C., et al. 2025a, arXiv e-prints, arXiv:2502.17556, doi: 10.48550/arXiv.2502.17556
Hoogendam, W. B., Ashall, C., Jones, D. O., et al. 2025b, arXiv e-prints, arXiv:2505.04610, doi: 10.48550/arXiv.2505.04610
Hosseinzadeh, G., Farah, J., Shrestha, M., et al. 2023, ApJL, 953, L16, doi: 10.3847/2041-8213/ace4c4
Huber, M., Chambers, K. C., Flewelling, H., et al. 2015, The Astronomer's Telegram, 7153, 1
Hughes, D. H., Dunlop, J. S., & Rawlings, S. 1997, MNRAS, 289, 766, doi: 10.1093/mnras/289.4.766
Hunter, J. D. 2007, Computing in Science and Engineering, 9, 90, doi: 10.1109/MCSE.2007.55
Ilee, J. D., Oudmaijer, R. D., Wheelwright, H. E., & Pomohaci, R. 2018, MNRAS, 477, 3360, doi: 10.1093/mnras/sty863
Inserra, C., Turatto, M., Pastorello, A., et al. 2011, MNRAS, 417, 261, doi: 10.1111/j.1365-2966.2011.19128.x
Itagaki, K. 2023, Transient Name Server Discovery Report, 2023-1158, 1
Iwata, Y., Akimoto, M., Matsuoka, T., et al. 2025, ApJ, 978, 138, doi: 10.3847/1538-4357/ad9a62
Jacobson-Galán, W. V., Dessart, L., Margutti, R., et al. 2023, ApJL, 954, L42, doi: 10.3847/2041-8213/acf2ec
Jakobsen, P., Ferruit, P., Alves de Oliveira, C., et al. 2022, A&A, 661, A80, doi: 10.1051/0004-6361/202142663
Janka, H.-T. 2012, Annual Review of Nuclear and Particle Science, 62, 407, doi: 10.1146/annurev-nucl-102711-094901
Janka, H.-T., Melson, T., & Summa, A. 2016, Annual Review of Nuclear and Particle Science, 66, 341, doi: 10.1146/annurev-nucl-102115-044747
Jencson, J. E., Pearson, J., Beasor, E. R., et al. 2023, ApJL, 952, L30, doi: 10.3847/2041-8213/ace618
Jerkstrand, A., Fransson, C., Maguire, K., et al. 2012, A&A, 546, A28, doi: 10.1051/0004-6361/201219528
Kendrew, S., Scheithauer, S., Bouchet, P., et al. 2015, PASP, 127, 623, doi: 10.1086/682255

Khokhlov, A., & Höflich, P. 2001, in American Institute of Physics Conference Series, Vol. 556, Explosive Phenomena in Astrophysical Compact Objects, ed. H.-Y. Chang, C.-H. Lee, M. Rho, & I. Yi (AIP), 301–312, doi: 10.1063/1.1368287
Kilpatrick, C. D., Foley, R. J., Jacobson-Galán, W. V., et al. 2023, ApJL, 952, L23, doi: 10.3847/2041-8213/ace4ca
Kotak, R., Meikle, P., van Dyk, S. D., Höflich, P. A., & Mattila, S. 2005, ApJL, 628, L123, doi: 10.1086/432719
Kotak, R., Meikle, P., Pozzo, M., et al. 2006, ApJL, 651, L117, doi: 10.1086/509655
Kotak, R., Meikle, W. P. S., Farrah, D., et al. 2009, ApJ, 704, 306, doi: 10.1088/0004-637X/704/1/306
Kumar, A., Dastidar, R., Maund, J. R., Singleton, A. J., & Sun, N.-C. 2025, MNRAS, 538, 659, doi: 10.1093/mnras/staf312
Kuncarayakti, H., Folatelli, G., Maeda, K., et al. 2020, ApJ, 902, 139, doi: 10.3847/1538-4357/abb4e7
Lantz, B., Aldering, G., Antilogus, P., et al. 2004, in Society of Photo-Optical Instrumentation Engineers (SPIE) Conference Series, Vol. 5249, Optical Design and Engineering, ed. L. Mazuray, P. J. Rogers, & R. Wartmann, 146–155, doi: 10.1117/12.512493
Law, D., Diaz, R., Sosey, M., et al. 2025, JWST Pipeline Notebooks, Tech. rep., doi: 10.5281/zenodo.15571377
Leonard, D. C., Filippenko, A. V., Gates, E. L., et al. 2002, PASP, 114, 35, doi: 10.1086/324785
Li, G., Wang, X., Yang, Y., et al. 2025, arXiv e-prints, arXiv:2504.03856, doi: 10.48550/arXiv.2504.03856
Li, H., & McCray, R. 1992, ApJ, 387, 309, doi: 10.1086/171082
Liljegren, S., Jerkstrand, A., & Grumer, J. 2020, A&A, 642, A135, doi: 10.1051/0004-6361/202038116
Liu, C., Chen, X., Er, X., et al. 2023, ApJL, 958, L37, doi: 10.3847/2041-8213/ad0da8
Liu, W., & Dalgarno, A. 1994, ApJ, 428, 769, doi: 10.1086/174285
—. 1995, ApJ, 454, 472, doi: 10.1086/176498
Liu, W., Dalgarno, A., & Lepp, S. 1992, ApJ, 396, 679, doi: 10.1086/171749
Lucy, L. B., Danziger, I. J., Gouiffes, C., & Bouchet, P. 1989a, in IAU Colloq. 120: Structure and Dynamics of the Interstellar Medium, ed. G. Tenorio-Tagle, M. Moles, & J. Melnick, Vol. 350, 164, doi: 10.1007/BFb0114861
—. 1989b, in IAU Colloq. 120: Structure and Dynamics of the Interstellar Medium, ed. G. Tenorio-Tagle, M. Moles, & J. Melnick, Vol. 350, 164, doi: 10.1007/BFb0114861
Maeda, K., Kawabata, K., Mazzali, P. A., et al. 2008, Science, 319, 1220, doi: 10.1126/science.1149437
Maguire, K., Di Carlo, E., Smartt, S. J., et al. 2010, MNRAS, 404, 981, doi: 10.1111/j.1365-2966.2010.16332.x
Maiolino, R., Schneider, R., Oliva, E., et al. 2004, Nature, 431, 533, doi: 10.1038/nature02930
Margutti, R., Soderberg, A. M., Chomiuk, L., et al. 2012, ApJ, 751, 134, doi: 10.1088/0004-637X/751/2/134
Martí-Devesa, G., Cheung, C. C., Di Lalla, N., et al. 2024, A&A, 686, A254, doi: 10.1051/0004-6361/202349061
Matheson, T., Filippenko, A. V., Barth, A. J., et al. 2000, The Astronomical Journal, 120, 1487
Maund, J. R. 2017, MNRAS, 469, 2202, doi: 10.1093/mnras/stx879
McCarthy, J. K., Cohen, J. G., Butcher, B., et al. 1998, in Society of Photo-Optical Instrumentation Engineers (SPIE) Conference Series, Vol. 3355, Optical Astronomical Instrumentation, ed. S. D'Odorico, 81–92, doi: 10.1117/12.316831
Medler, K., Ashall, C., Shahbandeh, M., et al. 2025, arXiv e-prints, arXiv:2505.18507, doi: 10.48550/arXiv.2505.18507
Meikle, W. P. S., Mattila, S., Pastorello, A., et al. 2007, ApJ, 665, 608, doi: 10.1086/519733
Meikle, W. P. S., Kotak, R., Farrah, D., et al. 2011, ApJ, 732, 109, doi: 10.1088/0004-637X/732/2/109
Mera, T., et al. 2025, ApJ, in prep.
Michel, P. D., Mazzali, P. A., Perley, D. A., Hinds, K. R., & Wise, J. L. 2025, MNRAS, 539, 633, doi: 10.1093/mnras/staf443
Milisavljevic, D., Fesen, R. A., Gerardy, C. L., Kirshner, R. P., & Challis, P. 2010, ApJ, 709, 1343, doi: 10.1088/0004-637X/709/2/1343
Modjaz, M., Kirshner, R. P., Blondin, S., Challis, P., & Matheson, T. 2008, ApJL, 687, L9, doi: 10.1086/593135
Müller, B., Heger, A., Liptai, D., & Cameron, J. B. 2016, MNRAS, 460, 742, doi: 10.1093/mnras/stw1083
Müller Bravo, T. E. 2023, temuller/idsred: First Release!, v0.1.0, Zenodo, doi: 10.5281/zenodo.7851772
Nayana, A. J., Margutti, R., Wiston, E., et al. 2025, ApJ, 985, 51, doi: 10.3847/1538-4357/adc2fb
Neustadt, J. M. M., Kochanek, C. S., & Smith, M. R. 2024, MNRAS, 527, 5366, doi: 10.1093/mnras/stad3073
Niculescu-Duvaz, M., Barlow, M. J., Bevan, A., et al. 2022, MNRAS, 515, 4302, doi: 10.1093/mnras/stac1626
Niu, Z., Sun, N.-C., Maund, J. R., et al. 2023, ApJL, 955, L15, doi: 10.3847/2041-8213/acf4e3
Oke, J. B., Cohen, J. G., Carr, M., et al. 1995, PASP, 107, 375, doi: 10.1086/133562
Panjkov, S., Auchettl, K., Shappee, B. J., et al. 2024, PASA, 41, e059, doi: 10.1017/pasa.2024.66

Park, S. H., Rho, J., Yoon, S.-C., et al. 2025, arXiv e-prints, arXiv:2507.11877, doi: 10.48550/arXiv.2507.11877

Pascual, S., Cardiel, N., Garzón, F., et al. 2019, in Astronomical Society of the Pacific Conference Series, Vol. 521, Astronomical Data Analysis Software and Systems XXVI, ed. M. Molinaro, K. Shortridge, & F. Pasian, 232

Pascual, S., Gallego, J., Cardiel, N., & Eliche-Moral, M. C. 2010, in Astronomical Society of the Pacific Conference Series, Vol. 434, Astronomical Data Analysis Software and Systems XIX, ed. Y. Mizumoto, K. I. Morita, & M. Ohishi, 353

Perley, D., & Gal-Yam, A. 2023, Transient Name Server Classification Report, 2023-1164, 1

Perrin, M. D., Sivaramakrishnan, A., Lajoie, C.-P., et al. 2014, in Society of Photo-Optical Instrumentation Engineers (SPIE) Conference Series, Vol. 9143, Space Telescopes and Instrumentation 2014: Optical, Infrared, and Millimeter Wave, ed. J. M. Oschmann, Jr., M. Clampin, G. G. Fazio, & H. A. MacEwen, 91433X, doi: 10.1117/12.2056689

Pledger, J. L., & Shara, M. M. 2023, ApJL, 953, L14, doi: 10.3847/2041-8213/ace88b

Podsiadlowski, P. 1992, PASP, 104, 717, doi: 10.1086/133043

Pozzo, M., Meikle, W. P. S., Fassia, A., et al. 2004, MNRAS, 352, 457, doi: 10.1111/j.1365-2966.2004.07951.x

Pozzo, M., Meikle, W. P. S., Rayner, J. T., et al. 2007, MNRAS, 375, 416, doi: 10.1111/j.1365-2966.2006.11298.x

Qin, Y.-J., Zhang, K., Bloom, J., et al. 2024, MNRAS, 534, 271, doi: 10.1093/mnras/stae2012

Ransome, C. L., Villar, V. A., Tartaglia, A., et al. 2024, ApJ, 965, 93, doi: 10.3847/1538-4357/ad2df7

Ravensburg, E., Carenza, P., Eckner, C., & Goobar, A. 2024, PhRvD, 109, 023018, doi: 10.1103/PhysRevD.109.023018

Ravi, A. P., Rho, J., Park, S., et al. 2023, ApJ, 950, 14, doi: 10.3847/1538-4357/accddc

Rayner, J. T., Toomey, D. W., Onaka, P. M., et al. 2003, PASP, 115, 362, doi: 10.1086/367745

Rho, J., Evans, A., Geballe, T. R., et al. 2021, ApJ, 908, 232, doi: 10.3847/1538-4357/abd850

Riess, A. G., Yuan, W., Macri, L. M., et al. 2022, ApJL, 934, L7, doi: 10.3847/2041-8213/ac5c5b

Roche, P. F., Aitken, D. K., & Smith, C. H. 1991, MNRAS, 252, 39P, doi: 10.1093/mnras/252.1.39P

Roche, P. F., Aitken, D. K., Smith, C. H., & James, S. D. 1989, Nature, 337, 533, doi: 10.1038/337533a0

Rockosi, C., Stover, R., Kibrick, R., et al. 2010, in Society of Photo-Optical Instrumentation Engineers (SPIE) Conference Series, Vol. 7735, Ground-based and Airborne Instrumentation for Astronomy III, ed. I. S. McLean, S. K. Ramsay, & H. Takami, 77350R, doi: 10.1117/12.856818

Sahu, D. K., Anupama, G. C., Srividya, S., & Muneer, S. 2006, MNRAS, 372, 1315, doi: 10.1111/j.1365-2966.2006.10937.x

Sarangi, A. 2022, A&A, 668, A57, doi: 10.1051/0004-6361/202244391

Sarangi, A., & Cherchneff, I. 2015, A&A, 575, A95, doi: 10.1051/0004-6361/201424969

Sarangi, A., Dwek, E., & Arendt, R. G. 2018, ApJ, 859, 66, doi: 10.3847/1538-4357/aabfc3

Sarmah, P. 2024, JCAP, 2024, 083, doi: 10.1088/1475-7516/2024/04/083

Scheck, L., Kifonidis, K., Janka, H. T., & Müller, E. 2006, A&A, 457, 963, doi: 10.1051/0004-6361:20064855

Schlafly, E. F., & Finkbeiner, D. P. 2011, ApJ, 737, 103, doi: 10.1088/0004-637X/737/2/103

Schneider, R., Ferrara, A., & Salvaterra, R. 2004, MNRAS, 351, 1379, doi: 10.1111/j.1365-2966.2004.07876.x

Shahbandeh, M., Hsiao, E. Y., Ashall, C., et al. 2022, ApJ, 925, 175, doi: 10.3847/1538-4357/ac4030

Shahbandeh, M., Sarangi, A., Temim, T., et al. 2023, MNRAS, 523, 6048, doi: 10.1093/mnras/stad1681

Shahbandeh, M., Ashall, C., Hoeflich, P., et al. 2024, arXiv e-prints, arXiv:2401.14474, doi: 10.48550/arXiv.2401.14474

Shahbandeh, M., Fox, O. D., Temim, T., et al. 2025, ApJ, 985, 262, doi: 10.3847/1538-4357/adce77

Shappee, B. J., Prieto, J. L., Grupe, D., et al. 2014, ApJ, 788, 48, doi: 10.1088/0004-637X/788/1/48

Sharp, C. M., & Hoeflich, P. 1990, Ap&SS, 171, 213, doi: 10.1007/BF00646849

Singh, A., Teja, R. S., Moriya, T. J., et al. 2024, ApJ, 975, 132, doi: 10.3847/1538-4357/ad7955

Singh, P. D. 1975, A&A, 44, 411

Sluder, A., Milosavljević, M., & Montgomery, M. H. 2018, MNRAS, 480, 5580, doi: 10.1093/mnras/sty2060

Smartt, S. J., Eldridge, J. J., Crockett, R. M., & Maund, J. R. 2009, MNRAS, 395, 1409, doi: 10.1111/j.1365-2966.2009.14506.x

Smith, N., Foley, R. J., & Filippenko, A. V. 2008, ApJ, 680, 568, doi: 10.1086/587860

Smith, N., Pearson, J., Sand, D. J., et al. 2023, ApJ, 956, 46, doi: 10.3847/1538-4357/acf366

Smith, N., Silverman, J. M., Filippenko, A. V., et al. 2012, AJ, 143, 17, doi: 10.1088/0004-6256/143/1/17

Snow, C. P., & Rideal, E. K. 1929, Proceedings of the Royal Society of London Series A, 125, 462, doi: 10.1098/rspa.1929.0179
Soraisam, M. D., Szalai, T., Van Dyk, S. D., et al. 2023, ApJ, 957, 64, doi: 10.3847/1538-4357/acef22
Spyromilio, J., & Leibundgut, B. 1996, MNRAS, 283, L89, doi: 10.1093/mnras/283.3.L89
Spyromilio, J., Meikle, W. P. S., Learner, R. C. M., & Allen, D. A. 1988, Nature, 334, 327, doi: 10.1038/334327a0
Stritzinger, M., Taddia, F., Fransson, C., et al. 2012, ApJ, 756, 173, doi: 10.1088/0004-637X/756/2/173
Stritzinger, M., Valerin, G., Elias-Rosa, N., et al. 2023, Transient Name Server AstroNote, 145, 1
Szalai, T., & Van Dyk, S. V. 2023, The Astronomer's Telegram, 16042, 1
Szalai, T., & Vinkó, J. 2013, A&A, 549, A79, doi: 10.1051/0004-6361/201220015
Szalai, T., Vinkó, J., Balog, Z., et al. 2011, A&A, 527, A61, doi: 10.1051/0004-6361/201015624
Szalai, T., Vinkó, J., Könyves-Tóth, R., et al. 2019, ApJ, 876, 19, doi: 10.3847/1538-4357/ab12d0
Taubenberger, S., Valenti, S., Benetti, S., et al. 2009, MNRAS, 397, 677, doi: 10.1111/j.1365-2966.2009.15003.x
Teja, R. S., Singh, A., Basu, J., et al. 2023, ApJL, 954, L12, doi: 10.3847/2041-8213/acef20
Thwaites, J., Vandenbroucke, J., Santander, M., & IceCube Collaboration. 2023, The Astronomer's Telegram, 16043, 1
Tinyanont, S., Lau, R. M., Kasliwal, M. M., et al. 2019, ApJ, 887, 75, doi: 10.3847/1538-4357/ab521b
Tinyanont, S., Fox, O. D., Shahbandeh, M., et al. 2025, ApJ, 985, 198, doi: 10.3847/1538-4357/adccc0
Tonry, J. L., Denneau, L., Heinze, A. N., et al. 2018, PASP, 130, 064505, doi: 10.1088/1538-3873/aabadf
Tucker, M. A., Shappee, B. J., Huber, M. E., et al. 2022, PASP, 134, 124502, doi: 10.1088/1538-3873/aca719
Tucker, M. A., Hinkle, J., Angus, C. R., et al. 2024, ApJ, 976, 178, doi: 10.3847/1538-4357/ad8448
Utrobin, V. P., & Chugai, N. N. 2009, A&A, 506, 829, doi: 10.1051/0004-6361/200912273
—. 2017, MNRAS, 472, 5004, doi: 10.1093/mnras/stx2415
Valiante, R., Schneider, R., Bianchi, S., & Andersen, A. C. 2009, MNRAS, 397, 1661, doi: 10.1111/j.1365-2966.2009.15076.x
van Breemen, J. M., Min, M., Chiar, J. E., et al. 2011, A&A, 526, A152, doi: 10.1051/0004-6361/200811142
Van Dyk, S. D., Szalai, T., Cutri, R. M., et al. 2024a, ApJ, 977, 98, doi: 10.3847/1538-4357/ad8cd8
Van Dyk, S. D., Srinivasan, S., Andrews, J. E., et al. 2024b, ApJ, 968, 27, doi: 10.3847/1538-4357/ad414b
Vasylyev, S. S., Yang, Y., Filippenko, A. V., et al. 2023, ApJL, 955, L37, doi: 10.3847/2041-8213/acf1a3
Virtanen, P., Gommers, R., Oliphant, T. E., et al. 2020, Nature Methods, 17, 261, doi: 10.1038/s41592-019-0686-2
Wang, T., & Burrows, A. 2024, ApJ, 962, 71, doi: 10.3847/1538-4357/ad12b8
Watson, D., Christensen, L., Knudsen, K. K., et al. 2015, Nature, 519, 327, doi: 10.1038/nature14164
Wesson, R., Barlow, M. J., Matsuura, M., & Ercolano, B. 2015, MNRAS, 446, 2089, doi: 10.1093/mnras/stu2250
Williams, B. F., Peterson, S., Murphy, J., et al. 2014, ApJ, 791, 105, doi: 10.1088/0004-637X/791/2/105
Wilson, J. C., Henderson, C. P., Herter, T. L., et al. 2004, in Society of Photo-Optical Instrumentation Engineers (SPIE) Conference Series, Vol. 5492, Ground-based Instrumentation for Astronomy, ed. A. F. M. Moorwood & M. Iye, 1295–1305, doi: 10.1117/12.550925
Wooden, D. H., Rank, D. M., Bregman, J. D., et al. 1993, ApJS, 88, 477, doi: 10.1086/191830
Woosley, S. E., Heger, A., & Weaver, T. A. 2002, Reviews of Modern Physics, 74, 1015, doi: 10.1103/RevModPhys.74.1015
Woosley, S. E., Pinto, P. A., & Ensman, L. 1988, ApJ, 324, 466, doi: 10.1086/165908
Woosley, S. E., & Weaver, T. A. 1995, ApJS, 101, 181, doi: 10.1086/192237
Xiang, D., Mo, J., Wang, L., et al. 2024, Science China Physics, Mechanics, and Astronomy, 67, 219514, doi: 10.1007/s11433-023-2267-0
Yamanaka, M., Fujii, M., & Nagayama, T. 2023, PASJ, 75, L27, doi: 10.1093/pasj/psad051
Zhang, J., Lin, H., Wang, X., et al. 2023, Science Bulletin, 68, 2548, doi: 10.1016/j.scib.2023.09.015
Zheng, W., Dessart, L., Filippenko, A. V., et al. 2025, ApJ, 988, 61, doi: 10.3847/1538-4357/ade0bf
Zimmerman, E. A., Irani, I., Chen, P., et al. 2024, Nature, 627, 759, doi: 10.1038/s41586-024-07116-6
Zsíros, S., Szalai, T., De Looze, I., et al. 2024, MNRAS, 529, 155, doi: 10.1093/mnras/stae507